

Frequency-dependent viscosity of xenon near the critical point

Robert F. Berg and Michael R. Moldover

Physical and Chemical Properties Division, National Institute of Standards and Technology, Gaithersburg, Maryland 20899-8380

Gregory A. Zimmerli*

NYMA Incorporated, 2001 Aerospace Parkway, Brook Park, Ohio 44142

(Received 9 March 1999)

We used a novel, overdamped oscillator aboard the Space Shuttle to measure the viscosity η of xenon near its critical density ρ_c and temperature T_c . In microgravity, useful data were obtained within 0.1 mK of T_c , corresponding to a reduced temperature $t = (T - T_c)/T_c = 3 \times 10^{-7}$. Because they avoid the detrimental effects of gravity at temperatures two decades closer to T_c than the best ground measurements, the data directly reveal the expected power-law behavior $\eta \propto t^{-\nu z_\eta}$. Here ν is the correlation length exponent, and our result for the viscosity exponent is $z_\eta = 0.0690 \pm 0.0006$. (All uncertainties are one standard uncertainty.) Our value for z_η depends only weakly on the form of the viscosity crossover function, and it agrees with the value 0.067 ± 0.002 obtained from a recent two-loop perturbation expansion [H. Hao, R.A. Ferrell, and J.K. Bhattacharjee, (unpublished)]. The measurements spanned the frequency range $2 \text{ Hz} \leq f \leq 12 \text{ Hz}$ and revealed viscoelasticity when $t \leq 10^{-5}$, further from T_c than predicted. The viscoelasticity's frequency dependence scales as $Af\tau$, where τ is the fluctuation-decay time. The fitted value of the viscoelastic time-scale parameter A is 2.0 ± 0.3 times the result of a one-loop perturbation calculation. Near T_c , the xenon's calculated time constant for thermal diffusion exceeded days. Nevertheless, the viscosity results were independent of the xenon's temperature history, indicating that the density was kept near ρ_c by judicious choices of the temperature versus time program. Deliberately bad choices led to large density inhomogeneities. At $t > 10^{-5}$, the xenon approached equilibrium much faster than expected, suggesting that convection driven by microgravity and by electric fields slowly stirred the sample. [S1063-651X(99)04210-5]

PACS number(s): 51.20.+d, 05.70.Jk, 64.60.Ht, 83.50.Fc

I. INTRODUCTION

As the liquid-vapor critical point is approached, the shear viscosity $\eta(\xi)$ measured in the limit of zero frequency diverges as ξ^{z_η} , where ξ is the correlation length, which itself diverges on the critical isochore as $t^{-\nu}$. [Here, $t = (T - T_c)$, T_c is the critical temperature, and $\nu = 0.630$.] The viscosity exponent z_η is central to the theory of dynamic critical phenomena [1]; the quantity $3 + z_\eta$ is called the "dynamic critical exponent," and it characterizes transport phenomena in all near-critical fluids with a scalar order parameter. Because the exponent $z_\eta \approx 0.069$ is so small, it is very difficult to measure accurately on Earth in a pure fluid such as xenon. Far from the critical point, the separation of the viscosity's divergent critical contribution from the analytic background contribution is uncertain because the critical contribution is a small fraction of the total and because the separation depends sensitively upon the "crossover function" $H(\xi)$, which is known only approximately. Close to the critical point, the very compressible xenon stratifies in the Earth's gravity and the divergence of the viscosity is blunted in a manner that depends upon the height of the viscometer. As illustrated by Fig. 1, stratification visibly blunted the divergence of the viscosity of xenon near $t_{\min} = 3 \times 10^{-5}$, even when the measurements were made using a high- Q oscillator only 0.7 mm high. The arguments of Ref. [2] show that t_{\min} scales with

the height h and the acceleration of gravity g as $(gh)^{0.64}$. Thus, a significant reduction of t_{\min} requires either a viscometer with $h \leq 0.7$ mm on Earth or the use of microgravity.

Here we report results obtained with a novel viscometer that we integrated into the "Critical Viscosity of Xenon" (CVX) experiment instrument and operated in 1997 aboard the Space Shuttle Mission STS-85. In the Shuttle's micro-

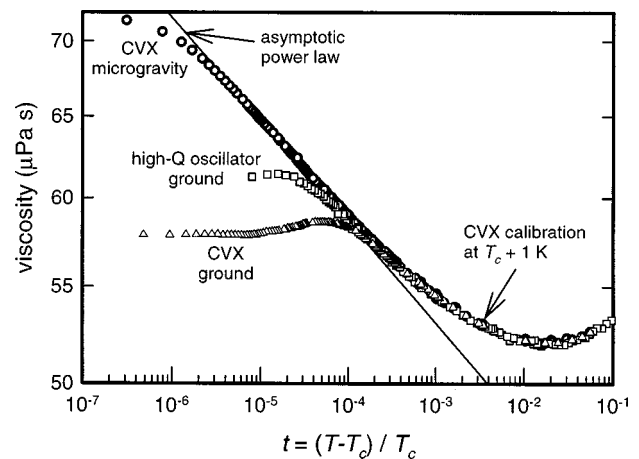


FIG. 1. Log-log plot of xenon's viscosity measured along the critical isochore near the critical point. The asymptotic line has the slope $z_\eta/\nu = 0.0435$ deduced from the present microgravity data. Near T_c , the CVX microgravity data [$\text{Re}(\eta)$ at 2 Hz] depart from the asymptotic line because of viscoelasticity. The two sets of ground data depart from the asymptotic line further from T_c because the xenon stratified in Earth's gravity.

*Present address: National Center for Microgravity Research, c/o NASA Glenn Research Center, MS 110-3, Cleveland, OH 44135.

gravity environment (approximately $1 \times 10^{-5} \text{ m s}^{-2}$), CVX obtained useful viscosity data at $t_{\min} = 3 \times 10^{-7}$, two decades in t closer to T_c than the best ground-based measurements. Indeed, the present data are useful closer to T_c than the data from any prior studies of liquid-vapor critical points, including those conducted in microgravity (e.g., [3–7]). The CVX data yielded a more accurate value of z_η than previous work, and they also produced the first accurate measurements of the frequency dependence of viscosity near any critical point. A short description of the viscoelasticity results was published earlier [8].

The CVX viscometer was a torsion oscillator that was driven at frequencies in the range $1/32 \text{ Hz} \leq f \leq 12 \text{ Hz}$. Both the in-phase and the quadrature components of the oscillator's response to the driving torque were measured. This permitted us to separately deduce the real and the imaginary components of the viscosity, $\text{Re}(\eta)$ and $\text{Im}(\eta)$. Both components are required to fully test theory [9]. The real component is the dissipative part of the response to shear stress that occurs in all fluids but superfluid helium. The imaginary component is the elastic part of the response that is ordinarily studied either at much higher frequencies or in complicated fluids such as polymer melts. In near-critical fluids, $\text{Im}(\eta) \neq 0$ when $f\tau \geq 1$, where f is the frequency of the measurement and τ is the fluctuation-decay time [1],

$$\tau = \frac{6\pi\eta\xi^3}{k_B T_c} = \tau_0 t^{-\nu(3+z_\eta)}, \quad (1)$$

where k_B is Boltzmann's constant. At the very low frequencies used by CVX, the viscoelastic behavior of xenon was evident when $t = 10^{-5}$ and it was dominant when $t = 10^{-6}$. (See Fig. 2.)

The theoretical model used to analyze the CVX data combined the scaling function $S(z)$ for near-critical viscoelasticity from Ref. [9], the crossover function $H(\xi)$ from Ref. [10], and the background viscosity η_0 from Appendix C of Ref. [11] to obtain the prediction

$$\eta(\xi, f) = \eta_0 \exp[z_\eta H(\xi)] [S(Az)]^{-z_\eta/(3+z_\eta)}. \quad (2)$$

[In the limits of large ξ and small f , $H(\xi) \sim \ln(\xi)$ and $S(z) = 1$, leading to $\eta \propto \xi^{z_\eta}$.] In Eq. (2), the scaled frequency is defined by $z = -i\pi f\tau$, and we introduced the parameter A into the argument of the scaling function $S(z)$ to obtain agreement with our data. Accurate measurements of the scaling function require accurate measurements of $\eta(\xi, f)$ in the region where ξ is large and where $|z|$ is varied through a large range from $|z| \ll 1$ to $|z| \gg 1$. Measurements prior to CVX were unable to achieve these conditions [12–15].

The CVX viscosity data at 2 Hz, 3 Hz, 5 Hz, 8 Hz, and 12 Hz were used to determine five parameters of Eq. (2). Two are the ‘‘universal’’ parameters z_η and A ; two are the fluid-specific wave vectors q_C and q_D that occur in the crossover function; and one is the value of T_c on CVX's temperature scale. When all of the data within the range $10^{-6} < t < 10^{-4}$ were fitted for these parameters, we obtained $z_\eta = 0.0690 \pm 0.0006$, $q_C \xi_0 = 0.051 \pm 0.007$, and $q_D \xi_0 = 0.16 \pm 0.05$. (The uncertainties indicated throughout this paper are one standard uncertainty and they allow for the correlations among the parameters.) The CVX result for z_η agrees with

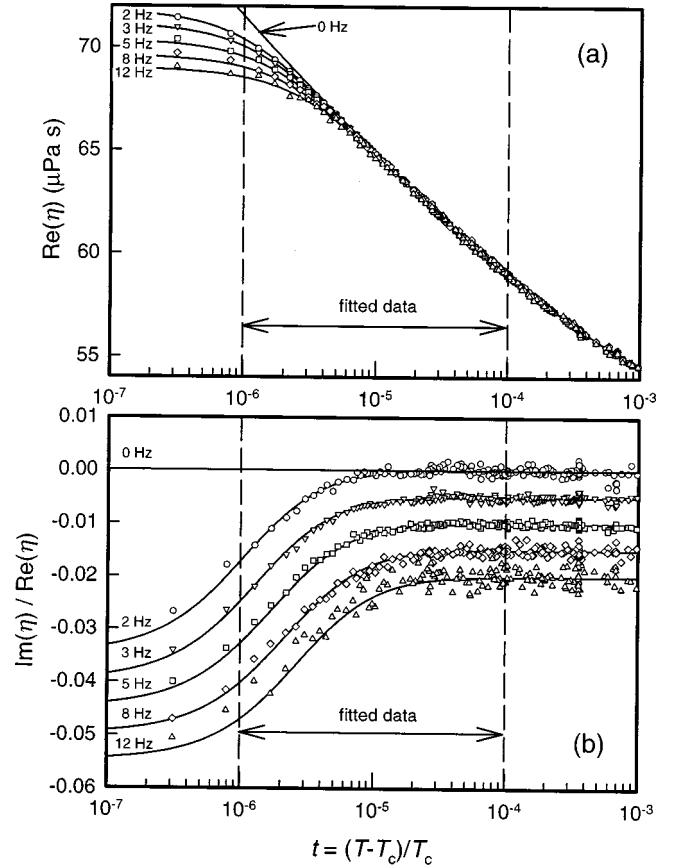


FIG. 2. Xenon's viscosity at critical density measured at frequencies from 2 to 12 Hz. The solid curves resulted from fitting Eq. (2) to the data in the range $10^{-6} < t < 10^{-4}$. (a) The real viscosity $\text{Re}(\eta)$. Near $t = 10^{-5}$, the data depart from the 0 Hz curve because of viscoelasticity. (b) The ratio $\text{Im}(\eta)/\text{Re}(\eta)$. For clarity, the ratio data at frequencies above 2 Hz are displaced downward by integer multiples of 0.005; otherwise they would coincide at $t > 2 \times 10^{-5}$.

the value $z_\eta = 0.067 \pm 0.002$ that was recently obtained from a two-loop perturbation expansion [16]. The CVX result for q_C agrees with the value $q_C \xi_0 = 0.059 \pm 0.004$ that we determined from independently published data that do not include the near-critical viscosity (Appendix D).

Figure 2(b) shows the ratio $\text{Im}(\eta)/\text{Re}(\eta)$. This ratio is independent of the background viscosity η_0 and of the crossover function $H(\xi)$, which are real common factors; thus, the ratio data are sensitive only to T_c and to the complex scaling function $S(Az)$. Figure 2 demonstrates that the functional form $S(Az)$ describes both $\text{Re}(\eta)$ and $\text{Im}(\eta)$ in the ranges $10^{-6} < t < 10^{-4}$ and $2 \text{ Hz} < f < 12 \text{ Hz}$, corresponding to $0.0004 < Az < 33$. The prediction that $\text{Im}(\eta)/\text{Re}(\eta)$ approaches approximately 0.035 for large values of z (see Appendix C) is consistent with these data. However, the value $A = 2.0 \pm 0.3$ resulting from the fit means that viscoelastic relaxation in xenon is two times slower than predicted by Bhattacharjee and Ferrell's one-loop calculation of $S(z)$ [9]. Their calculation implies $A = 1$ with no uncertainty estimate.

In orbit, the xenon sample did not have time to equilibrate fully at the smallest values of t because of critical slowing down. Thus, CVX's success depended upon programming the temperature as a function of time (the ‘‘temperature time-line’’) to ensure that temperature gradients within the xenon,

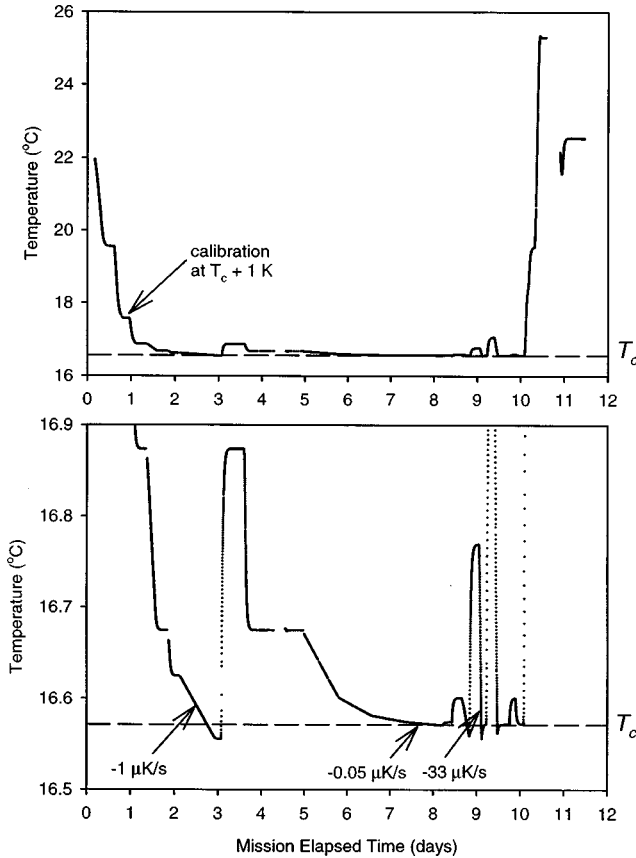


FIG. 3. The temperature timeline followed by CVX. Both panels show the same data but with different vertical scales.

which could cause deviations of the local density from the critical density ρ_c , were negligible. The timeline guaranteed that, in the xenon's interior where the viscosity was measured, the local density remained within 0.13% of the xenon's average density. The viscometer was not affected by the larger "piston-effect" density deviations that formed at the xenon's boundaries.

Key portions of the CVX data were taken as the temperature was ramped downward through T_c . As shown in Fig. 3, the first ramp, at the rate $-1 \mu\text{K s}^{-1}$, started at $T_c + 50 \text{ mK}$. The second ramp was 20 times slower; it started at $T_c + 3 \text{ mK}$ and had the rate $-0.05 \mu\text{K s}^{-1}$. Figure 4 shows that above T_c , the data from these two ramps superimpose within the noise. This is strong evidence that the temperature timeline was satisfactory. The xenon attained experimentally indistinguishable equilibrium states despite the very different temperature sequences preceding the ramps as well as very different ramp rates. Before the first ramp, the temperature sequence included equilibration at $T_c + 3 \text{ K}$ followed by a monotonic reduction of the temperature. Between the two ramps, the temperature was maintained at $T_c - 20 \text{ mK}$ for 2 h, long enough for macroscopic phase separation to have occurred, even in microgravity [7]. The procedure that caused the two ramps to produce equivalent data was the full equilibration of the xenon at $T_c + 100 \text{ mK}$ prior to each ramp. (See Fig. 3.) This temperature is sufficiently far from T_c that the xenon's equilibration time was acceptably short. This temperature is also sufficiently close to T_c that we could take advantage of the adiabatic constraint on the maximum density change that occurred during subsequent cooling to-

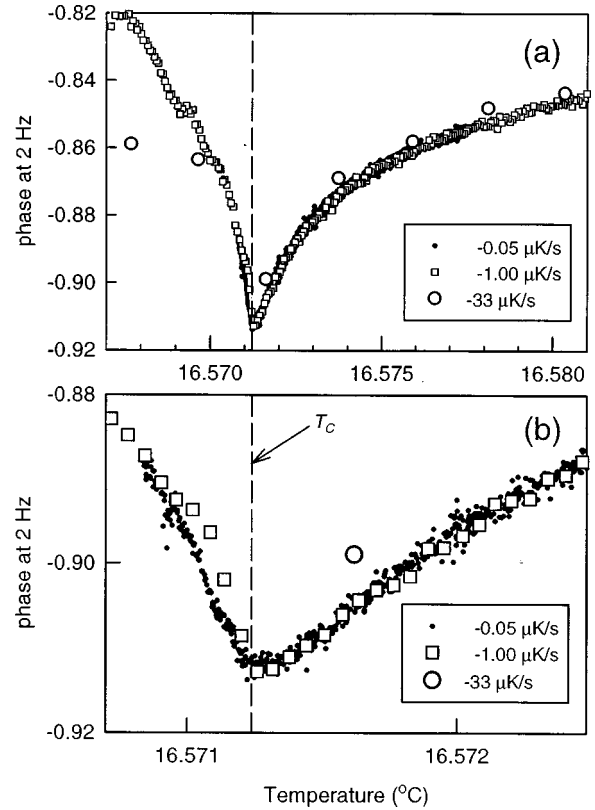


FIG. 4. Viscometer response as a function of temperature very near T_c . Both panels show data at three ramp rates. On the lower panel, the temperature scale is expanded by a factor of 8. (a) Above T_c , data collected at the fastest ramp rate of $-33 \mu\text{K s}^{-1}$ reflect the 0.3% lower density caused by starting the ramp at $T_c + 0.2 \text{ K}$. (b) Above T_c , data collected while ramping at $-0.05 \mu\text{K s}^{-1}$ agree with those collected five days earlier while ramping 20 times faster.

wards T_c . If the xenon were cooled adiabatically from $T_c + 100 \text{ mK}$ to T_c at *any* ramp rate, its density at the boundary would increase and its density in the interior would decrease by only $0.002\rho_c$. Calculations accounting for the diffusion of heat from the cooling xenon into the thermostat predicted that the density change during the slower ramp would be approximately half of the adiabatic constraint. (See Sec. III.) Our use of an equilibration procedure at $T_c + 100 \text{ mK}$ can be generalized and used to advantage in designing future microgravity experiments near liquid-vapor critical points.

As inferred from the viscometry, the xenon equilibrated faster than predicted by thermal diffusion. We believe this was caused by convection driven by the microgravity on the Shuttle and by the electric fields in the CVX cell. These small fields could couple to density differences to produce buoyant plumes up to several millimeters wide in the xenon surrounding the viscometer. Details appear in Sec. V A.

The CVX result $A = 2.0 \pm 0.3$ is a challenge to the theory; however, the challenge is comparable to one that Ferrell and Bhattacharjee met when scaling ultrasonic attenuation and dispersion in near-critical liquid mixtures. When they replaced the one-loop acoustic theory with a more sophisticated theory [17], the ultrasonic frequency scale changed by a factor of 1.6.

As discussed in Sec. V C, the CVX data determined the

product $A\tau_0 = 2.31 \pm 0.06$ ps with a relative uncertainty of 0.03. The relative uncertainty of A is larger (0.15) because of the uncertainty of the correlation length amplitude ξ_0 that propagated into τ_0 and then into $A\tau_0$. The uncertainty of A could be reduced by a factor of 5 if the uncertainty of ξ_0 were reduced, perhaps by additional measurements on Earth.

The present research was preceded by viscosity studies on Earth of xenon and carbon dioxide near their liquid-vapor critical points [11] and binary liquid mixtures near their consolute points [15]. The latter belong to the same dynamic universality class as pure fluids but are less influenced by gravity. We now identify the ways that CVX complements the previous research.

For tests of theory, i.e., Eq. (2), a simple pure fluid such as xenon has three advantages in comparison with binary liquid mixtures near consolute points. First, the dependences of the noncritical viscosity $\eta_0(\rho, T)$ on density ρ and temperature T are weak compared with the dependencies of $\eta_0(x, T)$ on mole fraction x and temperature for binary liquids. For pure fluids, the temperature dependence of $\eta_0(\rho, T)$ is indistinguishable from the well-understood dilute gas behavior $\eta_0(0, T)$ [20]. This means that $\eta_0(\rho, T)$ has a temperature dependence that is weaker than for binary liquids, and its use in fits to Eq. (2) adds no free parameters. Second, the fluid-dependent parameter q_C that appears in the crossover function $H(\xi)$ [10] is known for xenon; it has not been determined for any binary liquid. [The other parameter in $H(\xi)$ is the effective cutoff wave vector q_D that is used in a mode-coupling integral over momentum space. It is a free parameter related to the amplitude of the viscosity divergence.] Third, current technology allows the conditions of low frequency and shear rate to be met more easily with pure fluids than with liquid mixtures because the decay time τ of Eq. (1) is at least 100 times faster in pure fluids than in mixtures at the same reduced temperature.

Major divisions of the remainder of this manuscript are titled apparatus, temperature timeline, data reduction, and results. Appendixes deal with tabulated viscosity data, electrostriction, frequency-dependent scaling function $S(z)$, and estimation of q_C .

II. APPARATUS

The flight apparatus consisted of the cell containing the xenon sample and the oscillator, the surrounding thermostat, and the electronics, all carried within two flight canisters. Here we provide an overview. Additional details can be found in Refs. [18] and [19].

A. Oscillator and sample cell

The heart of the CVX viscometer, shown in Fig. 5, was an oscillator contained in a thick-walled copper sample cell. The oscillator was an 8×19 mm rectangle of screen that was cut out of a larger piece of nickel screen. The screen consisted of a square grid of 0.03-mm-wide wires formed by electrodeposition (Buckbee-Mears [21]) and spaced 0.85 mm apart. When the screen was cut, a wire was left extending from the middle of both of the rectangle's long edges. These two wires served as torsion springs, and they were soldered to a stiff yoke that was centered between four electrodes

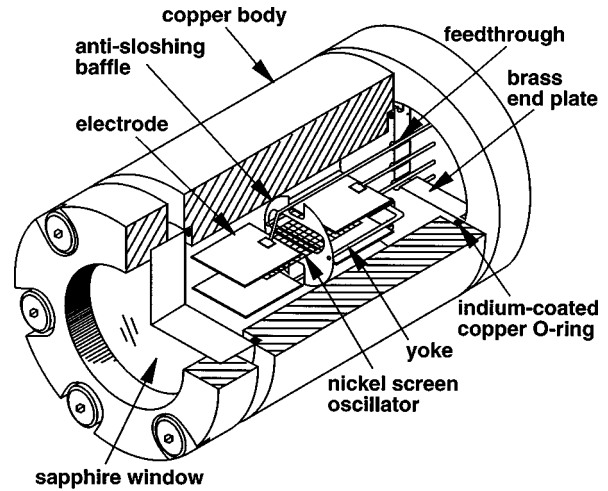


FIG. 5. Cutaway view of the CVX viscometer cell. The cylindrical volume occupied by the xenon was 38 mm long and 19 mm in diameter. Torque was applied to the screen by applying different voltages to diagonal pairs of electrodes while maintaining the screen at ground potential.

parallel to the screen. We chose the oscillator's dimensions so that it could be assembled by hand and so that it would be sensitive to changes of viscosity at low frequency. The oscillator's mass was approximately 1 mg.

Four electrodes were used to apply torque to the oscillator. To do so, diagonally opposite pairs of electrodes were charged to different voltages while the screen remained grounded. The resulting torque was a repeated, 32-s-long waveform with equally weighted frequency components in the range $1/32 \text{ Hz} < f < 12.5 \text{ Hz}$. Added to the torque voltages was a 10 kHz signal that allowed capacitive detection of the oscillator's motion. The electrodes were 10×12 mm rectangles of 0.13-mm-thick brass sheet soldered to 1-mm-diam wires that acted as both mechanical supports and as electrical leads. The electrodes lay in two planes located approximately 4 mm above and below the plane of the oscillator. The screen's yoke and the four electrodes were supported by feedthroughs in the brass end plate. The complete assembly was inspected for dust and then placed into the sample cell.

The sample cell had a 38 mm outer diameter and an inner, cylindrical space that was 38 mm long and 19 mm in diameter. One end of the cell was sealed by a sapphire window that had been coated with tin oxide to eliminate static charges. The other end was sealed by a brass plate containing five electrical feedthroughs connected to the oscillator and the four electrodes. The two sealing gaskets were made of indium-coated copper wire. The seals and feedthroughs were tested for leaks with a mass spectrometer leak detector while the cell was pressurized with helium at 12 MPa. The cell was heated to 100 °C, and pumped for 4 h to remove volatile contaminants; then it was cooled to room temperature and isolated from the vacuum pump. The oscillator's quality factor Q was monitored during the next four days. The time dependence of Q indicated that outgassing was negligible.

The torsion oscillator's resonance frequency f_0 , quality factor Q , and elastic aftereffect were measured in vacuum as functions of temperature. These measurements were used later in a model of the oscillator's anelasticity to predict the

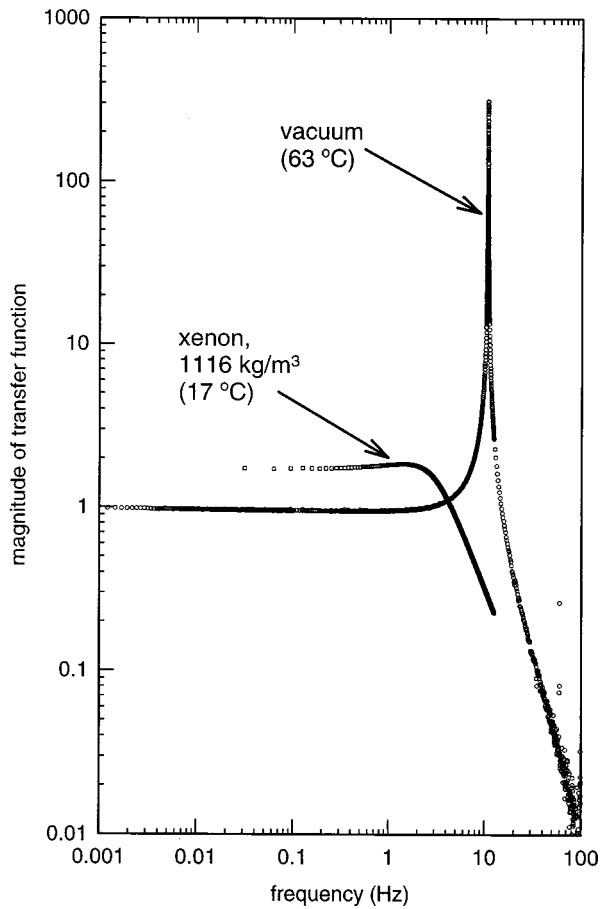


FIG. 6. The magnitude of the oscillator's transfer function measured in vacuum and in xenon at critical density.

frequency and temperature dependence of the oscillator's spring constant and its internal losses [22] at all frequencies. Near T_c , $f_0 \approx 11$ Hz and $Q \approx 1000$. See Fig. 6. No mode besides the torsion mode was detected at frequencies between 0 Hz and 100 Hz.

B. Xenon sample

Analysis of viscosity data close to T_c required accurate knowledge of the xenon's density. To ensure that the local density near the oscillator was within a few tenths of one percent of ρ_c , we controlled both the average density and the density gradients. The average density was fixed when the cell was loaded.

After characterization of the oscillator in vacuum, the sample cell was filled with xenon through a copper fill line. The manufacturer (Matheson [21]) stated that the xenon was 99.995% pure. To adjust the loading, the cell was immersed and held horizontally in a thermostated water bath at a temperature less than 2 mK below T_c . Xenon was added or removed to bring the liquid-vapor meniscus to the cell's mid-plane. The fill line was crimped, cut, and sealed by soldering. Epoxy was poured around the electrical feedthroughs as a precaution against leaks. The cell was weighed one year before and one year after the mission. The difference between the weighings indicated that less than 0.02% of the sample was lost during this period.

We measured the height of the meniscus when the sample was in equilibrium a few millikelvin below T_c . The inferred

average density was $\langle \rho \rangle = (0.9985 \pm 0.0017) \rho_c$. (We corrected for the volume of the fill line; asymmetries caused by the cell's internal parts were negligible.) Close to T_c , the difference $\rho - \rho_c$ limits the maximum correlation length, which in turn decreases the critical enhancement of viscosity. At the lower bound of the range of the fitted CVX data, $t = 1 \times 10^{-6}$, the corresponding decrease of the viscosity at 0 Hz was calculated to be $\eta(\xi(\rho_c)) - \eta(\xi(\langle \rho \rangle)) = (0.10_{-0.00}^{+0.36})\%$ (see Sec. V.B.1 of Ref. [15]).

We measured T_c by recording the temperatures at which the meniscus appeared and disappeared while the cell was immersed in the water bath. The thermometer was a standard platinum resistance thermometer (SPRT) immersed near the cell. (Further details are in Ref. [23].) Three years and one year before the mission, the respective values of T_c on the ITS-90 temperature scale were 289.731 ± 0.005 K and 289.734 ± 0.003 K, where the uncertainties bound the local variations in the water bath's temperature.

The xenon lowered the oscillator's Q from near 1000 to less than 1. This intentional overdamping made the viscometer insensitive to vibrations associated with normal Shuttle operations, and it led to other advantages. The overdamped oscillator was sensitive to viscosity changes in the range 2–12 Hz. This allowed the oscillator to be calibrated by exploiting a hydrodynamic similarity as described in Sec. IV B. The data at multiple frequencies provided a powerful check on the viscometer's accuracy, and they helped reveal the viscoelasticity of xenon near T_c . Finally, the overdamping made the oscillator rugged enough to survive the strong accelerations associated with launch and touchdown.

C. Thermostat

Maintaining adequate sample homogeneity near T_c required that temperature differences within the sample be less than $0.2 \mu\text{K}$. The CVX thermostat achieved such small temperature differences. It consisted of three coaxial aluminum shells surrounding the thick-walled copper sample cell. The cylindrical shells and their end caps were made from 6-mm-thick aluminum with a radial gap of 13 mm between shells. The large radial gap and stiff, glass-filled polycarbonate spacers between shells made the design mechanically robust and insensitive to errors of design and construction. The 38-mm separation between end caps allowed easy installation of the cell and its wiring. The weak coupling between shells that resulted from the large, nitrogen-filled gaps increased the thermostat's response time to more than 1 h. However, this was acceptable because the thermostat's response time was less than the sample's internal response time near the critical point. The thermostat's construction and operation are described in more detail elsewhere [18,19,24].

The performance of the thermostat was verified by using a semiconductor thermopile to measure the longitudinal temperature difference imposed along a thin-walled steel cell while controlling the thermostat at constant temperature and also while ramping it at $10 \mu\text{K s}^{-1}$ [24]. We extrapolated these results to CVX's thick-walled copper cell, including the calculated effect of the power dissipated by the thermistor. While ramping at the slowest rate of $-0.05 \mu\text{K s}^{-1}$, the maximum difference of the cell's wall

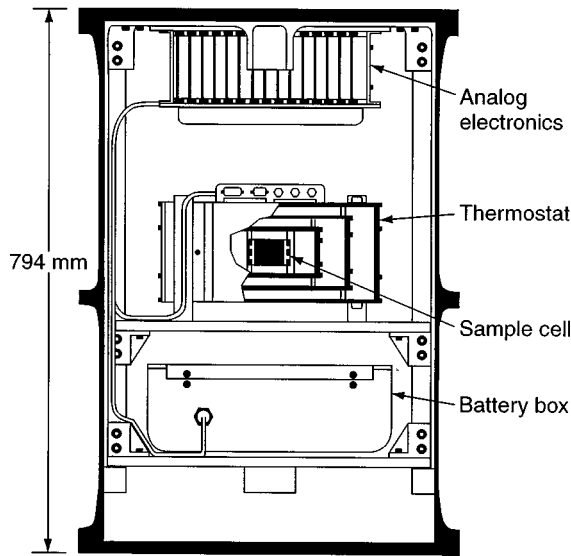


FIG. 7. Cross section of the experiment canister.

temperature from its average value was only $0.11 \mu\text{K}$. This corresponded to a density difference in equilibrium of $0.003\rho_c$ at $t = 1 \times 10^{-6}$, which was acceptable.

D. Flight canisters

The CVX flight instrument consisted of two sealed 0.8-m-tall aluminum ‘‘Hitchhiker’’ canisters connected to one another by a power/communications cable. The ‘‘experiment’’ canister, shown in Fig. 7, contained the thermostat and the more sensitive analog electronics. It also contained electrical batteries that were used to maintain the thermostat’s temperature above T_c during the Shuttle’s descent when no power was available. Keeping the sample above T_c during descent prevented the formation of liquid whose sloshing could have damaged the oscillator. The ‘‘avionics’’ canister contained power conditioners, an accelerometer, and the data acquisition and control electronics. It also contained the four computers dedicated to the tasks of viscometry, temperature control, accelerometry, and communications.

The canisters were mounted in the Space Shuttle’s payload bay, where the external heat load varied greatly depending on whether the open bay was oriented toward deep space, the Earth, or the Sun. These heat load variations changed the experiment canister’s interior temperature, which in turn affected the gain of the viscometry electronics. To minimize these temperature changes, the sides of the canister were thermally isolated and the mass of the canister’s lid was increased to 45 kg. A heater attached to the upper mounting plate, just below the underside of the lid, provided additional temperature control. Between mission days 1 and 10, the temperature of the experiment canister surrounding the thermostat was maintained within 1 K of 12°C .

The electronics and the thermostat were cooled only via radiation from the experiment canister’s lid. Thus, too large a heat load on the experiment canister would have caused a disastrous loss of thermostat control. Covering the canister lid with appropriate radiator tape and limiting the duration of the Shuttle’s bay-to-Sun orientations prevented this potential problem.

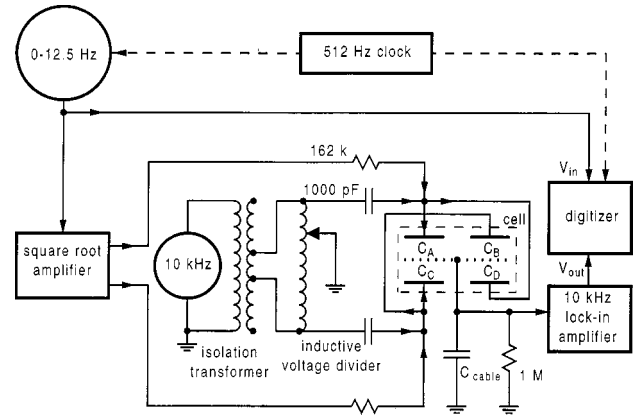


FIG. 8. Simplified diagram of the circuit used to drive and detect the oscillator’s motion.

E. Electronics

1. Oscillator drive voltages

The viscosity was deduced from the ratio $\tau_{\text{osc}}/\theta_{\text{osc}}$, where τ_{osc} is the torque applied to the oscillator and θ_{osc} is the resulting angular deflection. In the limit of large overdamping, the dependence of this ratio on frequency and viscosity was approximately

$$\frac{\tau_{\text{osc}}}{\theta_{\text{osc}}} \propto \rho f^2 B(R/\delta), \quad (3)$$

where R is an arbitrary length and

$$\delta \equiv \sqrt{\frac{\eta}{\pi \rho f}} \quad (4)$$

defines the viscous penetration length. Calibration determined the function $B(R/\delta)$. As described in this and in the following subsection, τ_{osc} and θ_{osc} were obtained from the measured input and output voltages, respectively. Then, as described in Sec. IV, viscosity was obtained by inverting an equation similar to Eq. (3).

Figure 8 is a schematic diagram of the circuit elements that were used to apply the torque and to measure the deflection. The paired $162 \text{ k}\Omega$ resistors and 1000 pF capacitors allowed the simultaneous presence at the electrodes of the subaudio frequency voltage used to drive the oscillator and the 10 kHz voltage used to detect the oscillator’s deflection. The $1 \text{ M}\Omega$ resistor at the input of the lock-in amplifier grounded the oscillator at low frequencies. A smaller resistor would have decreased the signal-to-noise ratio unacceptably, and a larger resistor would have prevented effective grounding. The interelectrode capacitances $C_A, C_B, C_C,$ and C_D shown in Fig. 8 were approximately 0.3 pF . This was much smaller than the cable capacitance C_{cable} ; however, the 10 kHz signal was still detected with a satisfactory signal-to-noise ratio.

In normal operation, the torque applied to the oscillator was proportional to a time-dependent voltage created by summing 400 equal-amplitude sine waves at frequencies evenly spaced from $f_1 = 1/32 \text{ Hz}$ to 12.5 Hz ,

$$V_{\text{in}}(t) = A \sum_{n=1}^{400} \sin[2\pi n f_1 t + \phi(n)]. \quad (5)$$

(In the analysis described in Sec. IV, data at multiple frequencies were averaged into 1-Hz bins.) This waveform had a period of 32 s. The phases $\phi(n)$ of the 400 components were chosen to minimize the waveform's maximum value of $|V_{\text{in}}(t)|/A$. A digital-to-analog converter with 16-bit voltage resolution and 512-Hz time resolution generated the waveform. A lowpass filter smoothed the waveform steps that occurred every 1/512 s. Occasionally, low-frequency measurements were made with a similar waveform whose duration was 512 s, and whose lowest frequency was $f_1 = 1/512$ Hz.

Because the electrostatic torque was proportional to the square of the drive voltages applied to the electrodes, we used analog circuits to transform the input voltage $V_{\text{in}}(t)$. A bias voltage V_{DC} was added to $V_{\text{in}}(t)$, and the square root of the sum,

$$V_1(t) = +V_{\text{DC}}\{1 + [V_{\text{in}}(t)/V_{\text{DC}}]\}^{1/2}, \quad (6)$$

was obtained. This voltage was applied to one of the diagonally connected electrode pairs (capacitances C_A and C_D). A similar voltage, but of opposite phase,

$$V_2(t) = -V_{\text{DC}}\{1 - [V_{\text{in}}(t)/V_{\text{DC}}]\}^{1/2}, \quad (7)$$

was applied to the other electrode pair (capacitances C_B and C_C). (The voltages V_1 and V_2 were given opposite signs because this was observed to reduce the nonlinearity of the torque with respect to V_{in} .) The total torque applied to the oscillator by the four electrodes was approximately

$$\frac{C_A V_{\text{DC}}^2 L_{\text{osc}}}{x_0} \left[\frac{V_{\text{in}}(t)}{V_{\text{DC}}} + \frac{x(t)}{x_0} \right], \quad (8)$$

where $L_{\text{osc}} \approx 19$ mm is the oscillator's length and $x(t)$ is the displacement at the oscillator's tip. The length of the gap between the oscillator and one electrode was $x_0 \approx 4$ mm; due to limitations of the construction technique, a smaller value would have caused unacceptable differences among the interelectrode capacitances.

The second term of Eq. (8) caused the electrostatic torque to increase linearly with the oscillator's displacement $x(t)$. The resulting small negative contribution to the oscillator's mechanical spring constant lowered the oscillator's resonance frequency f_0 . The correction for this "spring softening" is described in Sec. IV C. Terms of order $[x(t)/x_0]^2$ and higher were made negligible by the oscillator's small amplitude and by the approximate symmetry of the electrode pairs.

The square-root circuit made the torque on the oscillator very nearly a linear function of $V_{\text{in}}(t)$. It was necessary because the ratio $V_{\text{in}}/V_{\text{DC}}$ was as large as 0.2. This ratio could not be decreased significantly by increasing the bias voltage above its actual value, $V_{\text{DC}} = 30$ V. Such an increase of V_{DC} would have risked pulling the oscillator against one of the electrode pairs, and it would have added nonlinearity to the oscillator's equation of motion. The lowpass filter following the square-root circuit suppressed noise at 10 kHz.

2. Oscillator displacement detection

The oscillator's time-dependent displacement was detected by the unbalance of a capacitance bridge. See Fig. 8. The bridge was driven by a 3 V (rms), 10 kHz oscillator. An inductive voltage divider was adjusted to approximately balance the bridge. The out-of-balance signal was fed to a lock-in amplifier which generated a subaudio frequency voltage V_{out} that was linear in the difference of the capacitances

$$\Delta C(t) = (C_A + C_D) - (C_B + C_C). \quad (9)$$

This difference was approximately proportional to the oscillator's displacement $x(t)$.

$$\Delta C(t) \approx 4C_A \left(\frac{x(t)}{x_0} \right). \quad (10)$$

The viscometry's input and output signals, V_{in} and V_{out} , were processed in five steps. (i) Antialias filters removed frequencies above 128 Hz. (ii) The signals were simultaneously digitized at 512 Hz, in synchrony with the digital-to-analog converter which created $V_{\text{in}}(t)$. (iii) The resulting time records were Fourier transformed, and all but the 400 lowest frequencies were discarded, thereby digitally filtering the data. (iv) The function

$$G_{\text{meas}}(f) = \frac{\tilde{V}_{\text{out}}(f)}{\tilde{V}_{\text{in}}(f)}, \quad (11)$$

was computed from the ratio of the Fourier transforms of $V_{\text{in}}(t)$ and $V_{\text{out}}(t)$. We refer to $G_{\text{meas}}(f)$ as the viscometer's "transfer function" because $G_{\text{meas}}(f)$ is a dimensionless ratio describing the frequency response of a linear system. (v) This function was stored as 401 complex numbers. In normal operation, the 32 s of data collection were followed by 32 s during which the data were processed, stored, and transmitted to ground. The same 32 s waveform drove the oscillator during both halves of this 64 s cycle. The accuracy of the five signal processing steps was verified by constructing a passive lowpass filter with a transfer function that resembled that of the overdamped oscillator. The voltage $V_{\text{in}}(t)$ was applied to the filter instead of the square root circuit. The filter's transfer function measured by the CVX instrument agreed with that measured by a commercial spectrum analyzer (Hewlett Packard 35660A [21]). It also agreed with the transfer function calculated from the values of the filter's components.

The inductive voltage divider shown in Fig. 8 was developed by NIST's Electricity Division to fit on a single circuit card. Such a small size was possible because CVX's divider required only nine bits of resolution, many fewer than the 20 bits typical of commercial programmable dividers. The lock-in amplifier (Ithaco model 410 [21]) also fit on a single card.

3. Electric field effects

Electric fields drove the oscillator. Thus, they were essential to CVX's operation; however, they had two secondary effects.

First, the electric fields increased the xenon's local density via electrostriction. Electrostriction was of greatest con-

cern in the immediate vicinity of the oscillator because the oscillator's damping depended approximately upon a weighted integral of $\sqrt{\eta\rho}$ over a volume within a viscous penetration length of the oscillator's surface. Appendix B demonstrates that electrostriction had a negligible influence on CVX's operation because it increased the average density near the oscillator by less than $\Delta\rho/\rho_c=0.001$, the uncertainty in the sample's average density.

The second effect of the electric fields was electric-field-driven (dielectrophoretic) convection, which caused the parcels of the xenon that were more polarizable (because they were cooler and denser) to move toward regions of high electric field. Dielectrophoretic convection is analogous to the buoyancy-driven convection on Earth that transports cooler, denser regions that form near the top of a cell to the bottom of the same cell. In microgravity, such regions formed near the cell's boundary when the cell was cooled, and they formed in the cell's interior when the cell was warmed. Spinodal decomposition also caused their formation when the sample's temperature was brought below T_c . The characteristic pressure (chemical potential per unit mass) that drove dielectrophoretic convection in the gap between the oscillator and the electrodes was estimated as $P_E \approx 0.13$ mPa, four times greater than the hydrostatic pressure difference across the cell caused by Shuttle's typical microgravity (1×10^{-5} m s⁻²). (See Appendix B.)

4. Oscillator amplitude effects

Visual observations on the ground determined that the oscillator's maximum displacement was 0.03 mm at the tip of the screen. The resulting product $\dot{\gamma}\tau$ of shear rate $\dot{\gamma}$ and fluctuation-decay time τ was sufficiently low that CVX did not encounter near-critical shear thinning [25]. The oscillator dissipated approximately 7 pW in the xenon. The resulting rate of density change near the oscillator $\dot{\rho}$ was approximately proportional to the local power per unit volume \dot{Q}' and inversely proportional to xenon's heat capacity at constant pressure c_P . The estimate

$$\dot{\rho} = \frac{(\partial\rho/\partial T)_P}{\rho c_P} \dot{Q}', \quad (12)$$

integrated over the duration of the experiment, was negligible.

Increasing the oscillator's amplitude by a factor of 2 during ground tests demonstrated that the viscometer's response was independent of amplitude.

5. Temperature measurement and control

Each thermostat shell had an embedded thermistor whose temperature was measured once every eight seconds with a resistance bridge. The shell's temperature was controlled by a proportional-integral-derivative algorithm. The middle shell's temperature was set 0.03 K below that of the inner shell, and the outer shell was set 0.3 K below that of the middle shell.

The requirement that temperature differences within the sample be less than 0.2 μ K prevented use of a heater on the cell. Instead, the cell's temperature was controlled by controlling that of the surrounding inner shell. A thermistor em-

bedded in the cell's copper wall operated at a power of approximately 0.6 μ W. Its temperature was read by an ac bridge and lock-in amplifier.

By choosing each bridge's reference resistor to have a value near that of its thermistor at T_c , the need for an adjustable component, such as a ratio transformer, was eliminated. Temperature was inferred from the bridge's unbalance instead of from the adjustment required to balance the bridge. Far from T_c , the gain of the lock-in amplifier was decreased to accommodate the bridge's large unbalance. Within 50 mK of T_c , the rms scatter in the cell's apparent temperature was approximately 10 μ K over a few hours.

The cell's thermistor was calibrated against the inner shell's thermistor to simplify the cell's temperature control. The inner shell's thermistor calibration consisted of a fit of the Steinhart-Hart equation [26] to the resistances at 0 °C, 25 °C, and 50 °C. The manufacturer stated that these three calibration points had an uncertainty of 0.05 K. Thus, the uncertainty of the reduced temperature t was approximately 0.002 t , and temperature scale nonlinearity contributed negligible error to the derived value of the viscosity exponent. To independently test the calibration's accuracy, we compared the value $T_c=289.721$ K determined during the mission with the thermistor (Sec. VB 2) with the value $T_c=289.734 \pm 0.003$ K obtained one year earlier with the SPRT (Sec. IIB). To within 10 mK, the two values are consistent both with each other and with the value 289.74 ± 0.02 reported elsewhere for xenon [27]. The thermometry's stability was verified by comparing the temperature of the cell T_{cell} with that of the inner shell T_{in} . The difference $T_{\text{cell}} - T_{\text{in}}$ measured during the mission drifted less than 0.1 mK per day, and it differed from the difference measured nine months earlier by only 0.5 mK.

III. TEMPERATURE TIMELINE

The density of a pure fluid near its critical point is extremely sensitive to temperature gradients. For example, at ρ_c and $T_c + 1$ mK, the isobaric thermal expansivity of xenon is more than a million times larger than that of an ideal gas; thus even a tiny temperature gradient can induce a significant density gradient. In the absence of gravity, this effect limits the fluid's homogeneity.

On Earth, density gradients induced by temperature gradients are usually negligible in comparison to the much larger gradient induced by gravity. Furthermore, such gradients are short-lived because small values of thermal diffusivity are attained only in the small layer at the height where $\rho \approx \rho_c$. In contrast, density gradients induced in microgravity are long-lived because the sample's near-homogeneity allows very small values of thermal diffusivity throughout the sample. At $T_c + 1$ mK, the slowest time constant calculated for thermal diffusion in the CVX sample in the absence of convection was about one week [28].

CVX's conservative design did not rely on convection to ensure that the density would be sufficiently uniform. Instead, temperature gradients were minimized by careful design of the sample cell, the surrounding thermostat, and the sequence of temperature changes, or "temperature timeline." To keep the density near the oscillator acceptably close to the critical density ρ_c , the temperature timeline

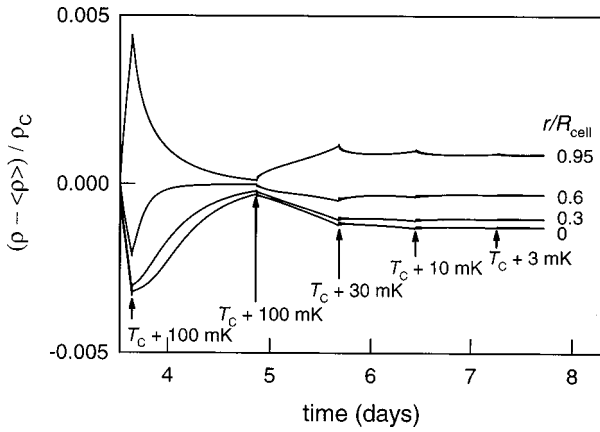


FIG. 9. The normalized density deviations calculated for a temperature timeline similar to that used by CVX. The arrows identify the boundary temperature at selected times. The sample is contained within an infinitely long cylinder with isothermal walls at radius $R_{\text{cell}}=9.5$ mm. Each curve represents the density at radius r . The density at the oscillator's location corresponds to the curve labeled "0," which represents the density on the cell's axis.

shown in Fig. 3 used a two-part strategy [28]. Far from T_c , the temperature was changed by large, rapid steps, causing large, temporary inhomogeneities in the sample. Each step was followed by a waiting period which exceeded the xenon's equilibration time constant and during which the density inhomogeneities decayed. Close to T_c , the xenon's temperature was changed without waiting for equilibrium; however, the density remained sufficiently close to ρ_c to obtain meaningful measurements of viscosity. This conclusion is supported by both calculations (this section) and observations (Sec. V A).

Candidate timelines were tested with a numerical model of entropy transport within the sample. The model contained two simplifications which allowed efficient testing. First, the xenon sample was modeled as an infinitely long cylinder whose density depended only on the radial coordinate r . In this approximation, the model was one-dimensional, and heat conduction through the cell's internal parts was ignored. Second, xenon's properties were estimated by an approximation to the cubic model equation of state. (The model is summarized in Ref. [2].) In this approximation, terms of order θ^2 and higher were dropped to remove the need for iterative calculations. The state parameter θ was always much less than 1. Figure 9 shows the density deviations calculated for a timeline similar to that used by CVX. The timeline specified the temperature changes at the cell's outer radius at $r=R_{\text{cell}}$. The resulting temperature differences within the sample were then converted into local-density differences at $r<R_{\text{cell}}$. Below T_c+100 mK, the density deviation in the cell's interior at $r=0$ was less than 0.13%. Heat conduction through the copper wires that supported the electrodes reduced this to less than 0.06%.

Our confidence in the model's physics came from a recent microgravity experiment [4], in which Wilkinson *et al.* demonstrated agreement between the measured and calculated values of thermal equilibration time constants in a sample of SF_6 near the critical point.

Our confidence in the coding was supported by comparing a simple numerical example with two analytic calculations.

The numerical example calculated the density change $\Delta\rho(t)$ in the sample's interior during and after a 2000 s ramp of the boundary temperature from $T_c+0.8$ K to $T_c+1.0$ K. During the ramp, $\Delta\rho(t)$ increased until it reached its maximum value at 2000 s. After the ramp, $\Delta\rho(t)$ decreased, with the decay becoming exponential after 8000 s.

The first analytic calculation was of thermal diffusion in an infinitely long cylinder, and it yielded the decay time constant for the cylinder's slowest radial mode. The analytic result of 5200 s agreed with the numerically calculated decay time constant.

The second analytic calculation was the adiabatic upper bound to the density change which occurs in the sample's interior following a sudden change of the cell wall's temperature from T_1 to T_2 . The analytic bound of $\Delta\rho=0.0022\rho_c$ agreed with the maximum numerical value of $\Delta\rho(t)$. (Thermal diffusion during the 2000 s ramp caused the maximum numerical value to be lower than the analytic bound by approximately 10%.)

The general expression for the adiabatic upper bound is

$$\frac{\Delta\rho}{\rho_c} \leq \int_{T_1}^{T_2} \left(\frac{\partial\rho}{\partial T} \right)_S dT \approx \frac{(\rho_c/P_c)}{(T_c/P_c)(\partial P/\partial T)_{\rho_c}} \int_{T_1}^{T_2} c_V dT, \quad (13)$$

where c_V is the constant-volume heat capacity. At times shortly after the wall's temperature change, this bound applies to all of the sample except for the thin layer associated with the piston effect near the wall. At later times and for locations in the sample's interior, the bound is still applicable because thermal diffusion causes the magnitude of the initial density deviation to decrease monotonically. Here, the interior is defined as the radius where the local temperature equals the sample's average temperature. If the CVX cell is modeled as a cylinder, this radius easily enclosed the oscillator because it lies at about two thirds of the cylinder's radius.

Equation (13) shows that changing the temperature from $T_c+0.1$ K to T_c induced changes of density in the sample's interior that were less than 0.2%. Because this constraint is independent of the rate of temperature change, the maximum temperature ramp near T_c was limited by other considerations. The ramp rate had to be slow enough that the viscosity would not change significantly during the time required to measure it.

The timeline used by CVX (Fig. 3) included the following features.

(i) Each temperature step was followed by a waiting period at constant temperature to observe the sample's approach to equilibrium.

(ii) The viscometer's calibration data were taken during the waiting period at T_c+1 K.

(iii) An initial "fast" temperature ramp passed through T_c at the rate $-1 \mu\text{K s}^{-1}$ and located T_c on the cell's thermometer to within 0.1 mK.

(iv) A later series of "slow" temperature ramps, the slowest of which passed through T_c at the rate $-0.05 \mu\text{K s}^{-1}$ and collected most of the data near T_c .

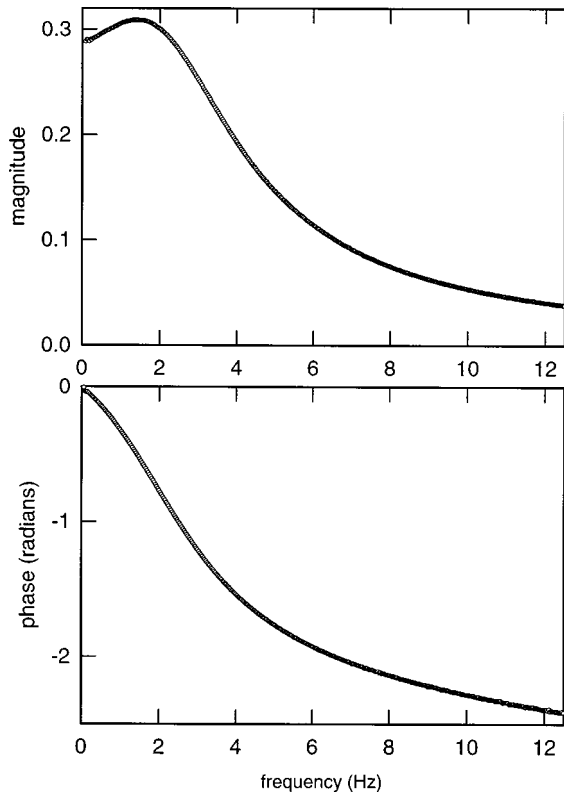


FIG. 10. The oscillator's transfer function $G_{\text{meas}}(f)$ measured at $T_c + 1$ K.

IV. DATA REDUCTION

During the mission, most data were downlinked in nearly real time for preliminary analysis, thereby allowing adjustments to the timeline. After the mission, all of the experimental data were retrieved from CVX's hard disk. They comprised approximately 10^4 measurements of the transfer function $G_{\text{meas}}(f)$, plus accompanying temperature measurements. Figure 10 shows typical measurements of the magnitude and phase of $G_{\text{meas}}(f)$. As described later in this section, we culled and averaged the data, then used a portion of the data from $T_c + 1$ K to calibrate the viscometer. Viscosity data were then derived from the averaged $G_{\text{meas}}(f)$ by combining the calibration with the model for the oscillator's equation of motion.

After the mission, data farther above T_c were collected. For these ground measurements, we calibrated the viscometer at $T_c + 5$ K instead of at $T_c + 1$ K because of concerns about internal waves at low frequencies in the gravitationally stratified xenon near T_c [29]. Appendix A lists viscosity values derived from the microgravity and ground measurements.

A. Culling and averaging of the data

The orbital environment influenced CVX in unexpected ways. Figure 11 shows $|G_{\text{meas}}(1 \text{ Hz})|$ measured during a 24-h period. The data include oscillations with a 45-min period and three "spikes" which lasted approximately 5 min each. Such oscillations and spikes occurred throughout the mission, and they affected the magnitude of the transfer function at all frequencies.

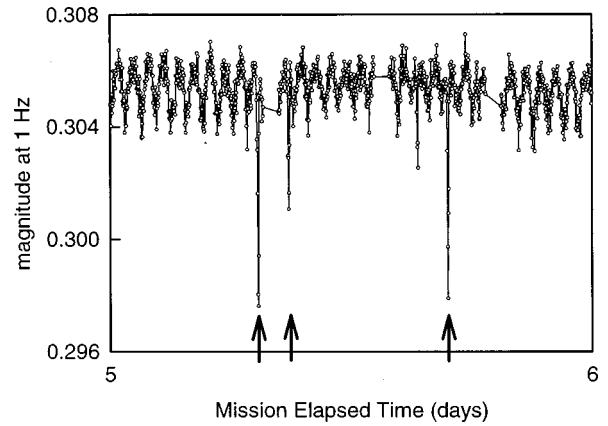


FIG. 11. Oscillations and spikes in the magnitude data at 1 Hz. The oscillation's 45-min period was half that of the Shuttle's orbital period. The minima of the oscillations occurred when the Shuttle crossed the Earth's equator. The three spikes indicated by arrows occurred when the Shuttle was near the South Atlantic Anomaly.

The oscillations' amplitude perturbed the apparent viscosity by as much as 0.4%. The oscillations' period was half of the Shuttle's orbital period, which suggests that they were not driven directly either by the Shuttle's exposure to the Sun or by the direction of the Earth's magnetic field. In ground tests, exposure of CVX to magnetic field variations comparable to those in orbit did not influence $G_{\text{meas}}(f)$. The oscillation minima occurred when the Space Shuttle was at high geomagnetic latitudes, which is consistent with the known distribution of the relativistic nucleon galactic cosmic ray flux that penetrates into low Earth orbit [30].

The spikes occurred when the Shuttle was near the South Atlantic Anomaly, a region of minimum magnetic field near Argentina. At this location, spacecraft in low Earth orbit experience a large increase in the flux of low-energy proton and electron particles trapped in the Earth's magnetosphere [31]. Thus, the timing of both the oscillations and the spikes, and their absence in ground tests of CVX, are consistent with the hypothesis that they were caused by ionization energy loss of charged particles in the xenon.

The oscillations and the spikes were present only in the magnitude data. We excluded measurements of $G_{\text{meas}}(f)$ obtained at the times of the spikes, and we suppressed the oscillations by averaging the remaining measurements in groups of 45 min. Each group was thus the average of up to 42 measurements. We did not weight the averaged $G_{\text{meas}}(f)$ by the number of measurements in each group. Instead, we simply excluded groups containing fewer than 30 measurements. The cell's temperature was averaged in a corresponding manner.

Figure 12 shows that the orbital environment also greatly increased the noise at frequencies below 0.1 Hz. In contrast to the oscillations and the spikes, this very low-frequency noise was present in both the phase and the magnitude, suggesting that either the sample, the oscillator, or both were directly affected. This in-orbit noise prevented our use of the low-frequency measurements for deriving the transducer factor k_{tr}/k_0 (see Sec. IV C).

In addition to data adversely affected by the orbital environment, we excluded data taken while the sample's density distribution was far from equilibrium. Such data were taken

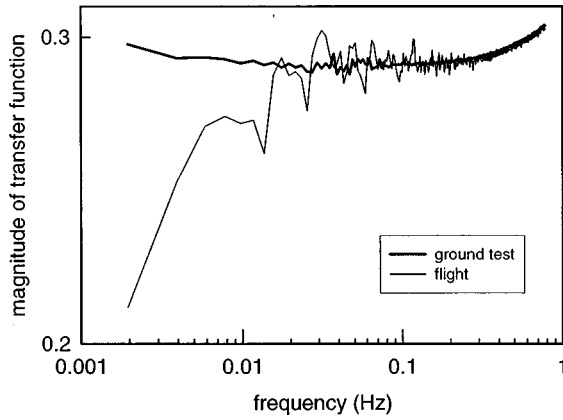


FIG. 12. Examples of the transfer function's magnitude measured at very low frequencies, where noise was much greater in orbit than on Earth.

below T_c and during and following large steps of temperature.

B. Hydrodynamic similarity and the viscometer's calibration

The viscometer's calibration exploited a hydrodynamic similarity which applies to the hydrodynamics of an immersed oscillator [32]. This analysis assumed that the fluid was homogeneous and that the oscillator moved as a rigid body. The similarity can be introduced by considering the response function of a damped harmonic torsional oscillator. The oscillator's response to a steady sinusoidal force at frequency f is given by

$$G(f) = \frac{1}{k} \left[1 - \left(\frac{f}{f_0} \right)^2 + \frac{i}{Q} \left(\frac{f}{f_0} \right) \right]^{-1}, \quad (14)$$

where k , Q , and f_0 are the oscillator's spring constant, quality factor, and undamped resonance frequency, respectively, and $G(f)$ is the ratio of the angular displacement of the oscillator to the external torque applied to the oscillator. By giving Q a frequency dependence appropriate for linearized hydrodynamics, this expression can describe the response of an immersed oscillator over a wide range of frequencies. For small amplitude oscillations, the response is

$$G(f) = \frac{1}{k} \left[1 - \left(\frac{f}{f_0} \right)^2 + i \left(\frac{f}{f_0} \right)^2 \left(\frac{\rho}{\rho_s} \right) B(R/\delta) \right]^{-1}, \quad (15)$$

where R and ρ_s are a characteristic length and density of the oscillator, respectively. The function $B(R/\delta)$ characterizes the oscillator's damping in terms of the viscous penetration length, defined by Eq. (3). At the nominal frequency of 5 Hz, $\delta \approx 60 \mu\text{m}$. Thus δ is larger than the nominal diameter of a screen wire ($2R = 28 \mu\text{m}$), but much less than the distance between wires ($847 \mu\text{m}$).

The viscosity enters $G(f)$ only through the function $B(R/\delta)$. Most oscillating-body viscometers are sensitive to viscosity changes only in a narrow range of frequencies near f_0 , and $B(R/\delta)$ must be calculated from the hydrodynamic theory for an idealized geometry. In contrast, we determined $B(R/\delta)$ by measuring $G(f)$ when the xenon was in a reference state of known η and ρ far from T_c and then inverting

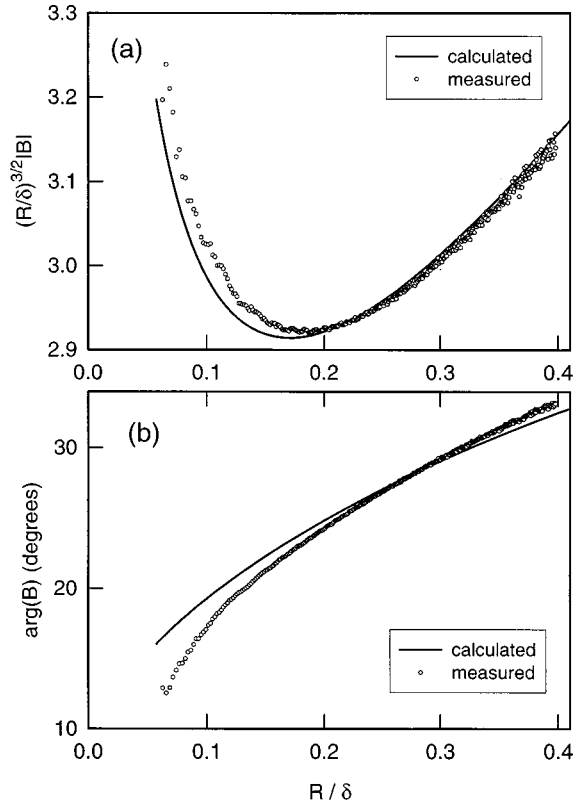


FIG. 13. The calibration function $B(R/\delta)$. The smooth curves indicate $B(R/\delta)$ calculated from the hydrodynamic theory of a transversely oscillating circular cylinder of radius $R = 13.4 \mu\text{m}$. (a) Magnitude scaled to reveal departures from the dominant $(R/\delta)^{3/2}$ behavior. (b) Phase.

Eq. (18) below. This procedure calibrated the viscometer for changes in the viscosity with respect to the reference viscosity. We emphasize that this calibration did not require knowledge of the geometry of either the oscillator or the surrounding electrodes, and it was indifferent to the choices of the parameters R and ρ_s . The accuracy of this technique was demonstrated in Ref. [32]. There, the viscosity of carbon dioxide was measured using a viscometer much like the CVX viscometer, and the results agreed with accurate published data acquired by conventional means.

The CVX viscometer's calibration was derived during the mission from an average of four 45-min measurements of $G_{\text{meas}}(f)$ obtained from 0 to 12.5 Hz at the average temperature $T_{\text{cal}} = T_c + 1.000 \text{ K}$. At this temperature, we equated the viscosity η_{cal} with that determined by the high- Q torsion oscillator, which had an uncertainty of 0.8%. (We multiplied the value obtained by fitting to Table IX of Ref. [11] by the ratio 1116/1110 to obtain $\eta_{\text{cal}} = 53.0 \mu\text{Pa s}$. The multiplication corrected for the lower value of ρ_c used to calculate Table IX.) After applying the corrections described below, useful values of $B(R/\delta)$ were derived from the transfer function at frequencies from 0.3 to 12.5 Hz, corresponding to a range of δ much broader than that encountered upon approaching T_c at fixed frequency. These values defined the calibration function $B_{\text{cal}}(R/\delta)$, whose magnitude and phase we represented by polynomial functions of $\ln(R/\delta)$ in the range $0.05 < R/\delta < 0.4$.

Figure 13 shows the measured values of $B(R/\delta)$ and an

approximation to $B(R/\delta)$ derived from an analytical model of the oscillator. This model is Stokes' solution for the viscous force exerted on a transversely oscillating cylinder. We used the modern formulation [33],

$$B_{\text{cyl}}(R/\delta) = -i \left[1 + \frac{4K_1(z)}{zK_0(z)} \right], \quad (16)$$

where $K_n(z)$ is the modified Bessel function of order n , and $z \equiv (1+i)(R/\delta)$. The small differences between $B_{\text{cyl}}(R/\delta)$ and $B(R/\delta)$ demonstrated that the oscillator's hydrodynamics resembled that of a single isolated cylinder. The influence of adjacent wires was small because δ was always much less than the distance between the screen's wires. Davis used his analytic calculation of an oscillating grid of flat wires to arrive at a similar conclusion [34]. We made no further use of either analytic model.

C. Corrections to the ideal transfer function

Figure 10 shows an example of the measured transfer function $G_{\text{meas}}(f)$, which is defined by Eq. (11). Our model of $G_{\text{meas}}(f)$ included several effects which caused $G_{\text{meas}}(f)$ to differ from the response $G(f)$ given by Eq. (15).

The largest effect was due to the driving and detection electronics shown in Fig. 8, which acted like a lowpass filter with a transfer function G_{elec} . The transfer function of the electronics G_{elec} was obtained by disconnecting the driving and detection stages from the cell and measuring their transfer functions independently. At the maximum frequency of 12.5 Hz, G_{elec} shifted the phase of $G_{\text{meas}}(f)$ by approximately 12° .

The oscillator's torsion spring was not ideal because slow relaxation processes within the nickel itself caused internal friction and creep. At the low amplitudes used in our measurements, these phenomena could be described as linear anelastic effects [22]. We corrected for anelasticity by generalizing the spring constant k to a complex function of frequency

$$k = k_0 [1 + \psi(f) + i\phi(f)], \quad (17)$$

where k_0 is the real part of the spring constant at the resonance frequency. The real functions $\psi(f)$ and $\phi(f)$ were measured in vacuum from 0.001 to 10 Hz at several temperatures [22].

Measurements in vacuum of the oscillator's resonance frequency f_0 as a function of temperature and bias voltage V_{DC} were used to obtain corrections of f_0 due to temperature and to filling the cell the cell with xenon. Filling the cell with xenon increased the capacitance C_A in Eq. (8). The resulting increase of electrostatic spring softening lowered f_0 by 0.4%. [The function $B(R/\delta)$ accounted for the xenon's effect on the oscillator's hydrodynamic mass.]

We did not correct $G_{\text{meas}}(f)$ to account for a second mode of the oscillator at higher frequency. A mode near 54 Hz, near the calculated bending frequency, was seen in vacuum measurements of a similar oscillator. However, no such mode was seen below 100 Hz with the CVX oscillator. Perhaps the bending mode was shifted to higher frequencies by stiffening caused by a slight intentional crease of the nickel screen.

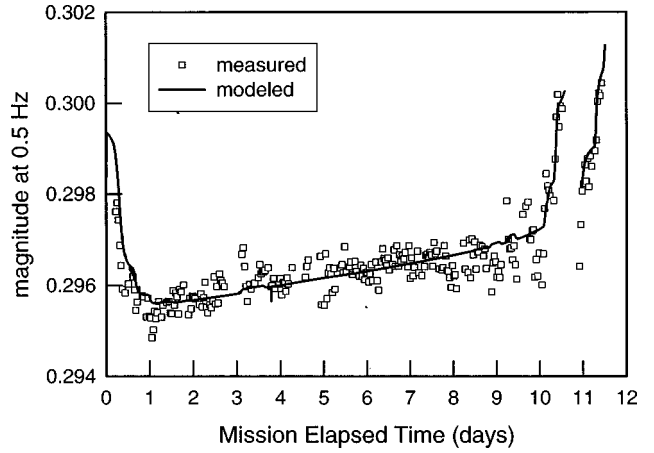


FIG. 14. The time dependence of the oscillator parameter k_{tr} . The solid curve is a fit to the transfer function's magnitude at 0.5 Hz, assuming that k_{tr} was a linear function of the cell's temperature, the experiment canister's temperature, and time.

With these corrections, the modeled transfer function becomes

$$G_{\text{meas}}(f) = G_{\text{elec}}(f) \left(\frac{k_{\text{tr}}}{k_0} \right) \left[1 + \psi(f) + i\phi(f) - \left(\frac{f}{f_0} \right)^2 + i \left(\frac{f}{f_0} \right)^2 \left(\frac{\rho}{\rho_s} \right) B(R/\delta) \right]^{-1}, \quad (18)$$

where k_{tr} is a real constant given by the product

$$k_{\text{tr}} = \left(\frac{\text{oscillator torque}}{\text{input voltage}} \right) \left(\frac{\text{output voltage}}{\text{oscillator displacement}} \right) \left(\frac{1}{G_{\text{elec}}} \right). \quad (19)$$

The product of the three transducer factors k_{tr} in Eq. (19) related the measured voltages $\tilde{V}_{\text{in}}(f)$ and $\tilde{V}_{\text{out}}(f)$ to the oscillator's torque and displacement.

Determination of the ratio k_{tr}/k_0 does not require accurate knowledge of k_0 or of the transducer factors. For example, in ground tests we obtained k_{tr}/k_0 from measurements of $G_{\text{meas}}(f)$ made near 0.01 Hz, where viscous damping was insignificant. To a good approximation, the derived value

$$\frac{k_{\text{tr}}}{k_0} \cong \frac{|G_{\text{meas}}(0.01 \text{ Hz})|}{1 - \psi(0.01 \text{ Hz})} \quad (20)$$

required knowledge of only the real part of the anelastic correction. In orbit, we were unable to measure k_{tr}/k_0 in a similar fashion because the signal-to-noise ratio of $G_{\text{meas}}(0.01 \text{ Hz})$ decreased by a factor of 10 or more. Instead, we set k_{tr}/k_0 to the value that made $\text{Re}(\eta)$ independent of frequency for $f > 1 \text{ Hz}$ in the temperature range $3 \times 10^{-5} < t < 5 \times 10^{-2}$ where viscoelastic effects were absent. This independence confirmed the assumption that k_{tr}/k_0 was independent of frequency. The in-orbit and ground values of k_{tr}/k_0 agreed within 0.3%.

The parameter k_{tr}/k_0 had linear dependences on the experiment canister's temperature, the cell's temperature, and time. The effects of these dependences can be seen in Fig. 14, which is a plot of $|G_{\text{meas}}(0.5 \text{ Hz})|$. At 0.5 Hz, $|G_{\text{meas}}|$ is

nearly independent of the sample's viscosity; thus, only unintentional dependences are present. The dependence on the experiment canister's temperature probably originated in the electronics; its coefficient was determined in ground tests. The dependence on the cell's temperature was assumed to result from the temperature dependence of the elastic constant of the torsion fiber and the thermal expansion of the capacitors. The torsion constant's temperature dependence was inferred from measurements of df_0/dT , and changes in the capacitance were determined by fitting $|G_{\text{meas}}(0.5 \text{ Hz})|$ to a linear function of the cell's temperature. The coefficient of the linear time dependence was determined by fitting to $|G_{\text{meas}}(0.5 \text{ Hz})|$. The origin of this time dependence was unknown. However, a similar time dependence occurred in $|G_{\text{meas}}(0 \text{ Hz})|$, which was linear in the oscillator's average displacement; both time dependences may have resulted from creep in the oscillator's equilibrium position.

D. Averaging with respect to frequency

Each 400-point transfer function was averaged into 1-Hz-wide frequency bins. For example, the value at 5 Hz was an average of the 33 points from 4.5 to 5.5 Hz. The simplest such average would have been

$$\langle G_{\text{meas}}(f) \rangle_0 \equiv \frac{\sum_{i=n-\Delta n}^{n+\Delta n} G_{\text{meas}}(f_i)}{(2\Delta n + 1)}, \quad (21)$$

where $n=160$ is the number of the point corresponding to 5 Hz and $\Delta n=16$. This (zeroth moment) average would have been inaccurate due to the nonlinear dependence of $G_{\text{meas}}(f)$ on f . Instead, we used a local parabolic fit to the data to define the average

$$\langle G_{\text{meas}}(f) \rangle = \frac{9\langle G_{\text{meas}}(f) \rangle_0 - 5\langle G_{\text{meas}}(f) \rangle_2}{4}, \quad (22)$$

where the curvature of $G_{\text{meas}}(f)$ was accounted for by the weighted (second moment) average

$$\langle G_{\text{meas}}(f) \rangle_2 \equiv \frac{\sum_{i=n-\Delta n}^{n+\Delta n} (f_i - f_n)^2 G_{\text{meas}}(f_i)}{\sum_{i=n-\Delta n}^{n+\Delta n} (f_i - f_n)^2}. \quad (23)$$

E. Derivation of viscosity from the transfer function

Derivation of the viscosity from $G_{\text{meas}}(f)$ required three steps. (i) Equation (18) was solved for $B(R/\delta)$ at frequency f . (ii) The complex value of δ was obtained from the complex value of $B(R/\delta)$ by iteratively comparing $B(R/\delta)$ with $B_{\text{cal}}(R/\delta_{\text{est}})$. Here $B_{\text{cal}}(R/\delta_{\text{est}})$ is the calibration function evaluated with an estimated penetration length δ_{est} . Using Newton's method, the value of δ_{est} was adjusted until $B_{\text{cal}}(R/\delta_{\text{est}}) = B(R/\delta)$. (iii) The viscosity was calculated from $\eta = \pi \rho f \delta_{\text{est}}^2$.

I. Complex viscosity

The above analysis generalizes to a fluid of complex viscosity because Eq. (15) was derived from hydrodynamics in the limit where the Navier Stokes equation is linear in velocity. Complex viscosity η causes the viscous penetration length δ to be complex; the generalization requires that the characterization of $B(R/\delta)$ for real arguments be extended to complex arguments. In principle, this extension could have been made by measuring $B(R/\delta)$ on a fluid with known, nonzero values of imaginary viscosity. In practice, such a calibration is impossible because only near-critical fluids are viscoelastic at the low viscosities and low frequencies used here. Instead of calibrating, we substituted a complex argument R/δ into the polynomials which characterized $B(R/\delta)$ for real viscosities. This substitution is the analytic continuation of $B(R/\delta)$ from the real line into the complex plane. The extrapolation was relatively small because the ratio $|\text{Im}(\eta)/\text{Re}(\eta)| < 0.04$.

2. Consistency of the data and correction of $\text{Im}(\eta)$

We checked the data reduction procedures by systematically varying various parameters from their nominal values. We changed the density by 1% from ρ_c . We changed the calibration viscosity by 3%. We changed the oscillator's vacuum resonance frequency by 3% from f_0 . We perturbed the transfer function G_{elec} used to describe the electronics. None of these variations caused significant changes in the data's consistency.

We used data outside the viscoelastic region ($t > 5 \times 10^{-5}$) to check the calibration procedure in three ways. First, the values of $\text{Re}(\eta)$ were examined at 2 Hz, 3 Hz, 5 Hz, 8 Hz, and 12 Hz for frequency dependence. None was found. Second, the values of $\text{Re}(\eta)$ were compared with our previous data [11] taken on Earth with a high- Q , 0.7-mm-high oscillating-cylinder viscometer. They agreed throughout the range $3 \times 10^{-4} < t < 5 \times 10^{-2}$, where the data sets overlap and where the high- Q data were not greatly affected by stratification. (The CVX data have a scatter of approximately 0.1%, and the high- Q data have a scatter of approximately 0.2%.) Third, the values of $\text{Im}(\eta)$ were examined for departures from zero. The examination revealed departures that were a weak function of $\ln(T - T_{\text{cal}})$, where $T_{\text{cal}} = T_c + 1 \text{ K}$ is the temperature at which the calibration function $B(R/\delta)$ was determined. The nonzero values of $\text{Im}(\eta)$ outside the viscoelastic region imply that the oscillator was influenced by an additional force inconsistent with the hydrodynamic similarity used to calibrate the viscometer.

Although the departures from zero of $\text{Im}(\eta)$ outside the viscoelastic region were less than $0.002 \text{ Re}(\eta)$, they were large enough to influence significantly the fitted value of A . Therefore, we corrected the data for $\text{Im}(\eta)$ as follows. At each frequency, we fit a function proportional to $\ln(T - T_{\text{cal}})$ to the values of $\text{Im}(\eta)$ well outside the viscoelastic region [$5 \times 10^{-5} < t < (T_{\text{cal}} - T_c)/T_c$]. [If we had assumed instead that the correction to $\text{Im}(\eta)$ was proportional to $(T - T_{\text{cal}})$ raised to a small power such as z_η , our results would have been unchanged.] After subtracting this function from the data, the values of $\text{Im}(\eta)$ were zero within their scatter. We then extrapolated this function from $t = 5 \times 10^{-5}$ towards T_c to correct the values of $\text{Im}(\eta)$ inside the viscoelastic region.

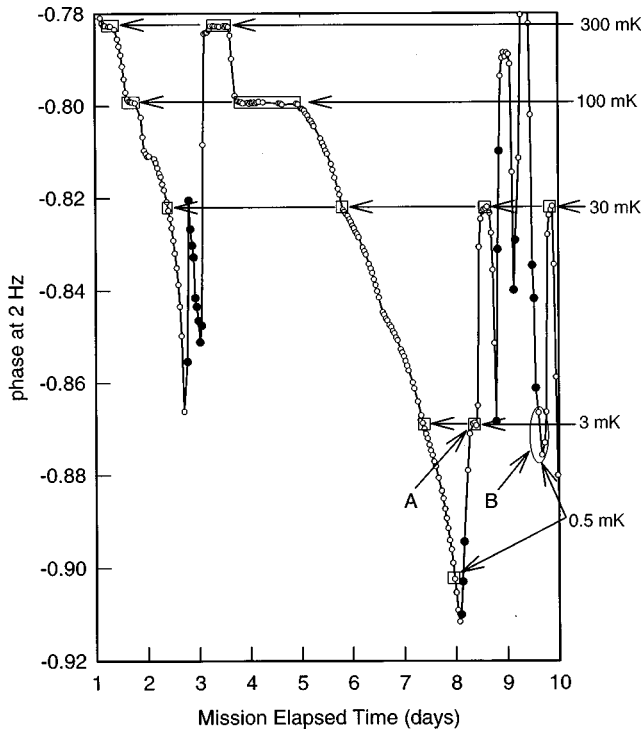


FIG. 15. The transfer function's phase at 2 Hz as a function of time. The boxes enclose measurements taken at the indicated temperatures, and their height corresponds to 0.2% of the density. The reproducibility of the oscillator's phase at 300 mK, 100 mK, 30 mK, and 3 mK above T_c demonstrates that density deviations could be reduced to within 0.1% of the average density at these temperatures. Filled points were obtained below T_c . The points denoted "A" and "B" were obtained shortly after warming the sample from below T_c . As discussed in the text, the equilibration of set B was much slower than that of set A.

We checked the validity of this extrapolation by fitting the parameter A separately to the values of $\text{Re}(\eta)$, which were not corrected, and to the corrected values of $\text{Im}(\eta)$. The two values of A agreed within 4%.

V. RESULTS

A. Sample homogeneity

1. History independence

Density inhomogeneities that were induced by temperature changes caused no apparent problems. Figure 15 supports this claim by showing the oscillator's phase measured at 2 Hz during a ten-day period. [We used the phase at 2 Hz because these data had a high signal-to-noise ratio and, unlike the magnitude data, they were unaffected by oscillations and spikes (Sec. IV A) or drift of k_{tr}/k_0 (Sec. IV C).] In Fig. 15, measurements made at 300 mK, 100 mK, 30 mK, and 3 mK above T_c are highlighted by boxes. At each temperature, measurements were repeated as much as seven days later and with very different temperature histories. The phase measurements agreed to within 1 mrad. This corresponds to an agreement in density of 0.1%.

Figure 4 shows that the sample's density could be kept near ρ_c even within 0.1 mK of T_c . Data collected during three ramps through T_c are shown. The slowest ramp, at

$-0.05 \mu\text{K s}^{-1}$, collected most of the data near T_c . The medium ramp, at $-1 \mu\text{K s}^{-1}$, was intended only to locate T_c to within 1 mK. Nevertheless, it gave results above T_c that were indistinguishable from those of the slowest ramp. Furthermore, after culling data points as described earlier, the data at higher temperatures also were independent of the sample's temperature history.

In Fig. 4, data from the fastest ramp at $-33 \mu\text{K s}^{-1}$ are displaced above and to the left of the equilibrium data. Because this ramp started at $T_c + 0.2 \text{ K}$, Eq. (13) indicates that the density of the xenon near the oscillator could have decreased by as much as 0.3%. This decrease is consistent with the data's vertical displacement. (Also, the thermometer's lag of several seconds caused a horizontal displacement of 0.1 mK.) Note also the ramp-rate dependence of the phase at 2 Hz below T_c . This time dependence is consistent with phase separation.

2. Equilibration

When the cell's temperature was held constant, the viscosity rapidly approached a steady value, typically within 1 h. (See Fig. 15.) Even after accounting for heat conduction through the cell's metal electrodes, this approach was faster than expected from the xenon's thermal diffusivity. At 300 mK, 100 mK, 30 mK, and 3 mK above T_c , the sample's calculated time constants for thermal relaxation were 1 h, 2 h, 6 h, and 30 h, respectively.

Three phenomena contributed to the rapid approaches to equilibrium. First, convection driven by residual accelerations (microgravity) and by electric fields slowly stirred the xenon. The stirring was effective because the open geometry around the oscillator reduced viscous damping of the convective flow. For example, if a density deviation $\Delta\rho = 0.01\rho_c$ had occurred in a region of characteristic size $L = 4 \text{ mm}$, an acceleration $g_{\text{micro}} = 10^{-6}$ of Earth's gravity would have turned over that portion of the sample in a time of order $\eta/(g_{\text{micro}}L\Delta\rho) \approx 3 \text{ min}$. Second, the oscillator was thermally isolated from the cell wall, and it had negligible heat capacity. Thus, following a temperature step above T_c , the density of the xenon immediately next to the oscillator changed by the same amount as that of the surrounding xenon and not by the much larger deviation that occurred near the cell's boundaries. For example, the initial density deviation in the cell's interior following the steps from $T_c + 300 \text{ mK}$ to $T_c + 100 \text{ mK}$ was calculated by Eq. (13) to be only 0.3%. Third, the oscillator was insensitive to deviations of the density from ρ_c if the deviations averaged to zero over the oscillator's surface. This insensitivity occurred because the oscillator's response was approximately proportional to the surface-averaged value of $\sqrt{\eta\rho}$ and, above $T_c + 1 \text{ mK}$ and for small deviations from ρ_c , the viscosity is proportional to the density.

To demonstrate the viscometer's sensitivity to density inhomogeneities, we deliberately created an inhomogeneous sample by cooling the cell to $T_c - 9 \text{ mK}$ and then warming it to $T_c + 0.5 \text{ mK}$. We then observed the apparent viscosity for 4 h. This set of observations is labeled "B" and enclosed by an oval in Fig. 15. It can be compared to the set labeled "A" that was cooled to $T_c - 0.5 \text{ mK}$ and then warmed to $T_c + 3 \text{ mK}$. Because xenon's calculated thermal diffusivity at

$T_c + 0.5$ mK is three times smaller than at $T_c + 3$ mK [28], one might expect the approach to equilibrium of set B to be three times slower than the approach of set A . Instead, the approach of set B was slower by much more than a factor of 3; the apparent viscosity differed from the equilibrium viscosity by 5% at the end of the 4-h observation.

One contribution to set B 's slower equilibration was the limited thermal conductance of the copper wire that connected each electrode to the cell wall. Below approximately $T_c + 1$ mK, the conductance of the copper wire was exceeded by that of the xenon between the electrode and the cell wall, and the length L_{thermal} that governed the sample's thermal diffusion was the cell's 19 mm diameter. In contrast, L_{thermal} for set A was the 8 mm gap between the electrodes.

Another possible contribution to set B 's slower equilibration was the size of its inhomogeneities. They were formed at $T_c - 9$ mK, where surface-tension-driven flows ensured that the liquid and vapor regions quickly grew as large as the sample's dimensions. In contrast, set A 's inhomogeneities were formed between T_c and $T_c - 0.5$ mK during a 2-h period; this is sufficiently brief that the liquid and vapor regions may not have had enough time to grow as large as the 8 mm interelectrode gap [7]. In that case, L_{thermal} was limited to the size of set A 's inhomogeneities, thereby speeding the decay of the inhomogeneities by thermal diffusion.

B. Fits to the data

1. Model of the data

Our model of the frequency-dependent data was Eq. (2). The frequency scaling function $S(z)$, including corrections to two typographic errors in Ref. [9], is given in Appendix C. We introduced the parameter A into the argument of the scaling function to obtain agreement with our data. Setting $A \equiv 1$ caused large systematic deviations from the fits.

In Eq. (2), the background viscosity was described by the sum of analytic functions of the density and the temperature:

$$\eta_0(T, \rho) = \eta_{00}(T) + \eta_{01}(\rho). \quad (24)$$

These functions were determined from the viscosity measured by others far from the critical point. (See Appendix C of Ref. [11].) For consistency with the measurements of Ref. [11], we set $\eta_0(T_c, \rho_c) = (51.3 \pm 0.4) \mu\text{Pa s}$. The present results are not sensitive to this description of η_0 . We used the value $\rho_c = 1116 \text{ kg m}^{-3}$ determined from Narger and Balzarini's sample no. 1 [35]. Both sample no. 1 and CVX used high-purity xenon from Matheson. We estimated the uncertainty of ρ_c as the difference of 1.3 kg m^{-3} between the values for sample Nos. 1 and 2.

Ideally the exponent characterizing the divergence of any thermophysical property would be determined from data so close to T_c that the critical anomaly is much larger than the noncritical background. The small value of the exponent z_η makes this impossible for viscosity, and the most accurate determination of z_η from the data requires knowledge of the crossover function $H(\xi)$. Recently, Luettmmer-Strathmann, Sengers, and Olchowy [36,37] published equations designed to describe the crossover behavior of both viscosity and thermal conductivity with a single fluid-dependent wave-number cutoff q_D . We used the older crossover function by Bhattacharjee *et al.* [10] for viscosity because it is simpler and has the same asymptotic behavior as the newer function. The older crossover function makes approximations not used in the newer function. The chief approximation is neglect of the divergence in the constant-volume heat capacity c_V [38]. Because we fitted to data only at reduced temperatures less than 10^{-3} , where the heat capacity ratio $c_V/c_P < 0.002$, this approximation introduced negligible errors.

The following subsections describe the results for T_c, z_η, A, q_c , and q_D obtained by fitting the model to the viscosity data. The fit included the values of $\text{Re}(\eta)$ and $\text{Im}(\eta)$ measured at 2 Hz, 3 Hz, 5 Hz, 8 Hz, and 12 Hz within the range $10^{-6} < t < 10^{-4}$. Expanding the range of fitted data to $10^{-6} < t < 10^{-3}$ caused negligible changes in the fitted parameters, while slightly increasing the fit's systematic deviations: The value of reduced χ^2 increased from 0.97 to 1.05.

2. Viscosity cusps near T_c

The fit of Eq. (2) ignored the data within 0.3 mK of T_c and yielded $T_c = (16.571\,237 \pm 0.000\,008) \text{ }^\circ\text{C}$, where the uncertainty is equivalent to $t = 3 \times 10^{-8}$. (Recall that, despite this precision, our thermometer's uncertainty with respect to ITS90 was 50 mK.) The standard uncertainties quoted here and below represent a coverage factor of 1 (68% confidence interval), and they allow for the correlations among the parameters. The phase and magnitude data exhibited cusps close to the fitted value of T_c . The minimum in the phase at 2 Hz shown in Fig. 4 is an example of such a cusp. As illustrated in Fig. 16, the phase at frequencies higher than 2 Hz exhibited a sharp local maximum. Table I lists the temperatures of three example cusps obtained by separate fits to data in a 2 mK span that included T_c .

Each value of T_{cusp} was determined to within $10 \mu\text{K}$. The values of T_{cusp} are thus mutually inconsistent even though they all differ from T_c by less than $60 \mu\text{K}$. Theory does not equate T_c with T_{cusp} because viscoelasticity and time-dependent phase separation determine T_{cusp} . Therefore, instead of using the values of T_{cusp} in the viscosity analysis, we allowed T_c to be a fitted parameter.

3. Viscosity exponent z_η

The viscosity exponent was obtained by dividing the fitted value, $\nu z_\eta = 0.043\,49 \pm 0.000\,35$, by the correlation length exponent, $\nu = 0.630$ [39,40], to obtain $z_\eta = 0.0690 \pm 0.0006$. This value for z_η is 7% larger than the value obtained from the high- Q torsion oscillator [11], even though the two data sets agree at $t > 3 \times 10^{-4}$, where gravity had a negligible influence on the high- Q data, and even though both data sets were analyzed with the same crossover function. The high- Q data led to a lower value of z_η because they were obtained at larger reduced temperatures, where the inaccuracy of the crossover function used here and in Ref. [11] is more important. Consistent with this attribution, fits to the present data at larger reduced temperatures yielded smaller values of z_η . These fits also showed systematic deviations that would not have been detected in the high- Q data because the latter had more noise.

Two recent papers by Hao, Ferrell, and Bhattacharjee have refined the theoretical estimate of z_η . The first paper

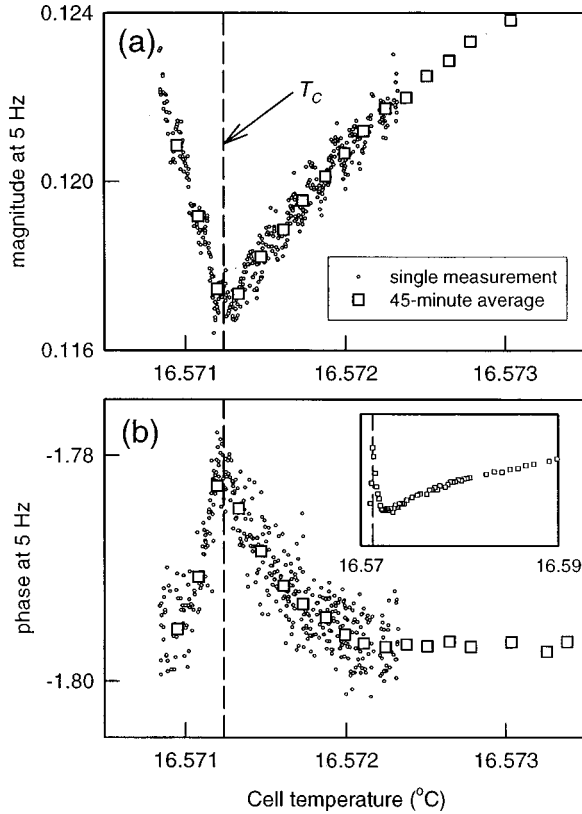


FIG. 16. Cusps in the data very close to T_c . These data were taken at 5 Hz; similar features occurred at other frequencies above 2 Hz. (a) Maximum damping (minimum amplitude) of the oscillator occurred within 0.01 mK of T_c , corresponding to $t = \pm 3 \times 10^{-7}$. (b) A maximum of the phase located within 20 μ K of T_c . The inset shows that the maximum was superposed on a broader minimum.

[41] is a mode coupling calculation of z_η in a two-term epsilon expansion. In contrast to earlier work by Siggia *et al.* [42], Hao *et al.* found that vertex corrections were significant, and they argued that a two-loop perturbation expansion in three dimensions would give a more accurate result. The second paper [16] gives the more accurate calculation, which leads to $z_\eta = 0.067 \pm 0.002$, where the uncertainty is the authors' "rough estimate of the inaccuracy introduced by various approximations." Thus the experimental and theoretical values of z_η agree within their combined uncertainties.

4. Viscoelastic time scale A

The value of A was obtained by replacing the fluctuation-decay time amplitude used in Eq. (2),

$$\tau_0 = \frac{6\pi\xi_0^3\eta_0}{k_B T_c [(q_C\xi_0)^{-1} + (q_D\xi_0)^{-1}]^{z_\eta}} = (1.15 \pm 0.17) \text{ ps}, \quad (25)$$

TABLE I. Cusps near T_c .

Cusp	$(T_{\text{cusp}} - T_c)/\mu\text{K}$
Phase at 2 Hz	+56
Magnitude at 5 Hz	-1
Phase at 5 Hz	-17

with the free parameter τ'_0 . This procedure yielded $\tau'_0 = (2.31 \pm 0.06)$ ps, thereby determining the frequency scale Az with a relative uncertainty of 0.03. However, the relative uncertainty of the ratio $A \equiv \tau'_0/\tau_0 = 2.0 \pm 0.3$ is 0.15 because of the larger uncertainty of τ_0 . The uncertainty of τ_0 is dominated by the uncertainty of xenon's correlation length amplitude, $\xi_0 = (0.184 \pm 0.009)$ nm, which we estimated as the difference between the two measurements reported by Güttinger and Cannell [43].

Bhattacharjee and Ferrell's theory of near-critical viscoelasticity [44,9] was stimulated by Bruschi *et al.*'s high-frequency measurements of viscosity near the critical point of CO_2 [12]. These measurements, and later measurements by Bruschi in CO_2 [13] and by Izumi *et al.* in xenon [14], showed only qualitative agreement with theory. Berg and Moldover's single-frequency measurements of two binary liquids required viscoelasticity in the analysis. (See Fig. 9 in [15].) However, the magnitude of the observable viscoelastic effect was only 0.5%; in hindsight we see that their data are consistent with $A > 1$.

In contrast to these previous measurements, the present data provide a quantitative test of the predicted functional forms. As shown by Fig. 2, the functional form $S(Az)$ describes the data for both $\text{Re}(\eta)$ and $\text{Im}(\eta)$ over a wide range of scaled frequency ($0.0004 < Az < 33$), provided that the viscoelastic time scale is adjusted by the factor $A = 2.0 \pm 0.3$. In particular, the description is consistent with the prediction that $\text{Im}(\eta)/\text{Re}(\eta)$ approaches 0.035 for large values of $|z|$.

5. Wave vectors q_C and q_D

Fitting to the logarithms $\ln(q_C\xi_0)$ and $\ln(q_D\xi_0)$ instead of $q_C\xi_0$ and $q_D\xi_0$ made the fitting routine more robust. The values obtained were $q_C\xi_0 = 0.051 \pm 0.007$ and $q_D\xi_0 = 0.16 \pm 0.05$. The fitted value of $q_C\xi_0$ agrees with the independent value 0.059 ± 0.004 determined from published data that do not include the near-critical viscosity. See Appendix D.

ACKNOWLEDGMENTS

We thank the CVX development team led by A.M. Peddie and J.L. Myers at NYMA Inc., the TAS-01 Mission team led by N.F. Barthelme, and the STS-85 crew. We thank R.A. Ferrell, R.W. Gammon, and R.A. Wilkinson for stimulating and critical comments. D.G. Friend's careful reading of the manuscript led to many improvements. The CVX project was managed by R.W. Lauer and I. Bibyk through the NASA Lewis Research Center and was funded by the NASA Microgravity Science and Applications Division.

APPENDIX A: TABULATED VISCOSITY DATA

Tables II and III give values of $\text{Re}(\eta)$ outside the viscoelastic region. Only data taken at 2 Hz are listed. The data at higher frequencies were consistent with those at 2 Hz; however, they had smaller signal-to-noise ratios. Three of the values represent a single 45-min data point, and their uncertainty σ_1 was estimated as the standard deviation of all of the 45-min points from a fit to the data in the range $10^{-6} < t < 10^{-3}$. (All three have $\sigma_1 \approx 0.03$.) The other values

TABLE II. CVX data taken in microgravity ($t > 2 \times 10^{-5}$).

$10^5 t$	$\text{Re}[\eta(2 \text{ Hz})]/(\mu\text{Pa s})$
1029.0	52.241 ± 0.017
344.3	53.009 ± 0.018
104.1	54.509 ± 0.010
100.0	54.585 ± 0.013
96.35	54.576 ± 0.022
65.51	55.213 ± 0.018
59.60	55.275 ± 0.032
43.36	55.923 ± 0.023
35.89	56.305 ± 0.010
35.48	56.339 ± 0.010
34.76	56.349 ± 0.013
29.69	56.709 ± 0.012
21.18	57.359 ± 0.024
20.76	57.389 ± 0.015
17.07	57.824 ± 0.012
14.93	58.080 ± 0.017
11.73	58.658 ± 0.017
11.03	58.784 ± 0.024
8.645	59.291 ± 0.024
8.620	59.351 ± 0.011
6.808	59.876 ± 0.025
5.886	60.246 ± 0.014
4.978	60.610 ± 0.025
4.381	60.937 ± 0.018
3.142	61.765 ± 0.025
2.960	61.930 ± 0.011
2.211	62.713 ± 0.018

are averages of N 45-min points, and their uncertainty was estimated as σ_1 / \sqrt{N} .

Table IV gives values of $\text{Re}(\eta)$ and $\text{Im}(\eta)/\text{Re}(\eta)$ inside the viscoelastic region. Each temperature represents a single 45-min data point. The uncertainties, which depend on fre-

TABLE III. CVX data taken on the ground ($t > 1 \times 10^{-3}$).

$10^5 t$	$\text{Re}[\eta(2 \text{ Hz})]/(\mu\text{Pa s})$
5527	52.623 ± 0.015
3976	52.316 ± 0.012
2420	52.073 ± 0.017
1730	52.047 ± 0.021
1729	52.048 ± 0.010
1729	52.048 ± 0.010
1729	52.047 ± 0.010
1729	52.053 ± 0.017
1039	52.178 ± 0.017
1034	52.162 ± 0.017
354.2	52.928 ± 0.031
338.0	52.974 ± 0.015
220.9	53.446 ± 0.031
140.9	54.011 ± 0.022
105.6	54.375 ± 0.011
105.4	54.360 ± 0.010

quency but not temperature, are listed at the head of each column.

The values in the tables are based on the value $\eta_{\text{cal}} = 53.0 \mu\text{Pa s}$ assumed for the viscosity at the calibration temperature $T_c + 1.000 \text{ K}$. The value of η_{cal} is uncertain by 0.8%.

APPENDIX B: ELECTROSTRICTION

A time-independent electric field of magnitude E that is localized to a small volume of the xenon causes a relative increase in the local density given by

$$\frac{\Delta\rho}{\rho_c} = \left(\frac{P_E}{P_c}\right) \chi_T^*. \quad (\text{B1})$$

Here $P_E = (\epsilon_{\text{Xe}}/\epsilon_0 - 1)(\epsilon_{\text{Xe}}/\epsilon_0 + 2)\epsilon_0 E^2/6$ is the induced change in chemical potential per unit mass [45], P_c is xenon's critical pressure, and ϵ_0 and ϵ_{Xe} are the permittivities of vacuum and xenon. Electrostriction is conspicuous near T_c because of the large density changes resulting from the large value of χ_T^* , the reduced susceptibility at constant temperature.

As a first step toward calculating E , we ignored the oscillator's presence and modeled the electric field between the viscometer's driving electrodes as that in a parallel plate capacitor. See Fig. 17. If the voltages on the two electrodes are V_1 and V_2 , and the distances from the oscillator to the two electrodes are x_1 and x_2 , this electric field's magnitude is

$$E_0 = \frac{(V_1 - V_2)}{(x_1 + x_2)}. \quad (\text{B2})$$

Electrostriction due to E_0 was insignificant.

Next we modeled the field concentrated near one of the thin wires comprised by the oscillator. We adapted Spangenberg's [46] model for the electric potential in a vacuum tube, consisting of two electrodes and a grid modeled as a planar array of parallel line charges. The radial field E_r near one of the wires, modeled as a cylinder, is

$$E_r(r, \theta) = (E_1 + E_2) \left(\frac{a}{4\pi r}\right) + E_0 \left[1 + \left(\frac{R}{r}\right)^2\right] \cos(\theta). \quad (\text{B3})$$

Here r and θ are cylindrical coordinates centered on the wire, R is the radius of the wire, and $a \gg R$ is the spacing between wires. The first term in Eq. (B3) originates in the wire's

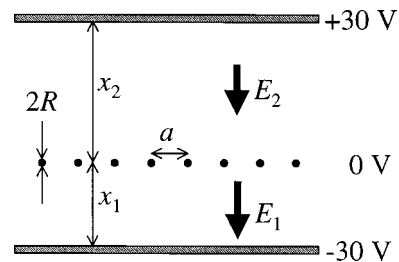


FIG. 17. Model cross section of the CVX electrodes used to calculate electric fields. The field near the screen depended on the potentials V_1 and V_2 , the distances x_1, x_2 , and a , and the wire radius R .

TABLE IV. CVX viscoelastic data ($t < 2 \times 10^{-5}$).

$10^6 t$	$\text{Re}(\eta)/(\mu\text{Pa s})$					$-10^4 \text{Im}(\eta)/\text{Re}(\eta)$				
	2 Hz	3 Hz	5 Hz	8 Hz	12 Hz	2 Hz	3 Hz	5 Hz	8 Hz	12 Hz
	± 0.04	± 0.04	± 0.05	± 0.07	± 0.11	± 8	± 6	± 4	± 8	± 15
19.91	63.00	63.00	62.99	63.04	62.92	5	9	7	17	11
18.91	63.14	63.13	63.12	63.09	62.94	6	8	-1	9	4
16.63	63.46	63.47	63.41	63.51	63.47	7	2	8	25	7
15.70	63.62	63.64	63.63	63.60	63.55	9	7	11	12	28
13.80	63.96	63.97	63.99	63.91	63.95	5	7	15	17	-13
12.72	64.18	64.18	64.17	64.23	63.93	-8	9	12	31	15
11.92	64.33	64.36	64.36	64.37	64.19	5	13	18	12	10
11.03	64.33	64.53	64.50	64.50	64.36	2	12	11	31	23
10.27	64.71	64.72	64.70	64.66	64.66	9	14	18	42	56
9.76	64.83	64.84	64.84	64.85	64.62	5	15	20	29	51
9.27	64.83	64.99	64.98	64.99	64.79	5	12	24	39	58
8.84	65.13	65.11	65.06	65.06	64.81	5	15	16	50	3
8.38	65.27	65.26	65.26	65.16	65.27	2	15	22	47	24
7.87	65.43	65.42	65.40	65.40	65.35	9	17	32	43	17
7.41	65.58	65.57	65.53	65.48	65.24	3	19	26	53	72
6.97	65.77	65.79	65.70	65.71	65.57	18	21	20	40	45
6.21	66.09	66.08	66.05	65.95	65.83	17	28	40	64	63
5.34	66.47	66.49	66.38	66.41	66.11	22	32	43	62	62
4.88	66.77	66.74	66.68	66.63	66.56	39	45	57	82	76
4.40	67.00	67.01	66.93	66.90	66.43	28	44	58	92	115
3.95	67.31	67.30	67.28	67.12	66.81	38	56	69	94	103
3.49	67.64	67.60	67.46	67.25	67.11	48	63	71	107	118
3.02	68.00	67.95	67.81	67.59	67.45	55	79	84	113	111
2.60	68.37	68.25	68.17	67.93	67.51	77	98	102	145	123
2.19	68.82	68.74	68.53	68.19	67.58	90	110	131	157	175
1.69	69.38	69.24	68.92	68.56	68.22	111	131	155	178	222
1.28	69.94	69.71	69.39	68.85	68.60	143	169	187	207	198
0.79	70.65	70.33	69.81	69.36	68.68	179	213	237	265	253
0.31	71.43	70.98	70.39	69.71	69.05	268	290	300	319	306

induced line charge, and it disappears when the fields $E_1 \equiv V_1/x_1$ and $E_2 \equiv V_2/x_2$ are equal and opposite. It is a factor of two smaller than in Spangenberg's model because the charge induced on the CVX oscillator was spread over transverse as well as longitudinal wires. The second term originates in the wire's induced line dipole; it was added to Spangenberg's model to create a zero potential surface at $r=R$.

We applied Eq. (B3) to CVX using the values $a = 0.85$ mm, $R = 0.009$ mm, and $V_1 = -V_2 = V_{\text{DC}} = 30$ V. We allowed for asymmetry in the viscometer's construction by estimating the unequal distances $x_1 = 3$ mm and $x_2 = 5$ mm. At the wire's surface, the field was concentrated by the factor $E_r/E_0 = 6$. At $T_c + 0.3$ mK, the associated density increase was only 0.05% and thus negligible.

APPENDIX C: FREQUENCY-DEPENDENT SCALING FUNCTION $S(z)$

Bhattacharjee and Ferrell calculated the frequency-dependent viscosity of a classical fluid near its critical point. The relevant portion of their results in Ref. [9] is reproduced here, correcting two typographic errors in the original published expressions for $\ln(S_4)$ and for $R(z)$.

The dependence of the viscosity on correlation length ξ and frequency f is

$$\eta(\xi, f) = \eta(\xi, 0) S^{-z_\eta/(3+z_\eta)}, \quad (\text{C1})$$

where the argument of the scaling function $S(z)$ is the scaled frequency defined by $z \equiv -i\pi f\tau$. Bhattacharjee and Ferrell used the decoupled-mode theory to calculate $S(z)$ to single-loop order. They accurately approximated their result in closed form by an average of calculations in two and four dimensions,

$$S \approx (\tilde{S}_2)^{2/3} (\tilde{S}_4)^{1/3}. \quad (\text{C2})$$

Here, the tilde refers to additional rescalings given by

$$\tilde{S}_2(z) \equiv S_2((2/e)^3 z) \quad \text{and} \quad \tilde{S}_4 \equiv S_4((8/e)z). \quad (\text{C3})$$

The scaling functions S_2 and S_4 are given by

$$\ln(S_2) = \left(\frac{z}{z-1} \right) + \left(\frac{z}{z-1} \right)^2 \ln z \quad (\text{C4})$$

and

$$\ln(S_4) = \left(-3 + \frac{2}{z}\right) + \left(1 - \frac{3}{z} + \frac{1}{z^2}\right) \ln z + \left(5 - \frac{5}{z} + \frac{1}{z^2}\right) R(z), \quad (\text{C5})$$

where

$$R(z) = \left(\frac{1}{(1-4z)^{1/2}}\right) \ln\left(\frac{1+(1-4z)^{1/2}}{1-(1-4z)^{1/2}}\right), \quad |z| < \frac{1}{4}, \quad (\text{C6})$$

$$R(z) = \left(\frac{1}{(4z-1)^{1/2}}\right) \tan^{-1}[(4z-1)^{1/2}], \quad |z| \geq \frac{1}{4}.$$

In the limit of large $|z|$, the ratio of imaginary and real viscosities approaches the value

$$\frac{\text{Im}(\eta)}{\text{Re}(\eta)} = \tan \frac{\pi z \eta}{2(3+z\eta)} \approx 0.0353, \quad |z| \rightarrow \infty. \quad (\text{C7})$$

APPENDIX D: ESTIMATION OF Q_C

The dimensionless parameter $q_C \xi_0$ is given by [10]

$$q_C \xi_0 = \frac{k_B P_c \Gamma^+}{16 \eta_0 \lambda_0 \xi_0} \left[\frac{T_c}{P_c} \left(\frac{\partial P}{\partial T} \right)_{\rho_c} \right]^2 = 0.059 \pm 0.004, \quad (\text{D1})$$

TABLE V. Quantities used to calculate q_C .

Quantity			Uncertainty (%)	Reference
T_c	289.74	K	0.01	[27]
P_c	5.83	MPa	0.2	[27]
ρ_c	1116	kg m ⁻³	0.1	[35]
Γ^+	0.058		3.5	[47]
ξ_0	0.184	nm	4.9	[43]
η_0	51.3	$\mu\text{Pa s}$	0.8	[11]
λ_0	0.0166	W K ⁻¹ m ⁻¹	2.5	[48]
$(T_c/P_c)(\partial P/\partial T)_{\rho_c}$	5.65		2.9	[27]

where η_0 and λ_0 are the background viscosity and thermal conductivity, and Γ^+ is the amplitude of the reduced compressibility. Table V gives the values and uncertainties used in Eq. (D1).

The references for λ_0 and $(\partial P/\partial T)_{\rho_c}$ did not give uncertainties. We estimated the value and uncertainty of $(\partial P/\partial T)_{\rho_c}$ from Table XXVIII and Fig. 14, respectively, of Ref. [27]. We obtained λ_0 by interpolating the plot in Ref. [48]. We estimated the uncertainty of λ_0 from the agreement between the thermal conductivity values λ at atmospheric pressure and the prediction $\lambda = 15k_B \eta/(4m)$, where m is the molecular mass.

- [1] P.C. Hohenberg and B.I. Halperin, Rev. Mod. Phys. **49**, 435 (1977).
- [2] M.R. Moldover, J.V. Sengers, R.W. Gammon, and R.J. Hocken, Rev. Mod. Phys. **51**, 79 (1979).
- [3] R.W. Gammon, J.N. Shaumeyer, M.E. Briggs, H. Boukari, D. Gent, and R.A. Wilkinson, *Proceedings of the 1997NASA/JPL Microgravity Fundamental Physics Workshop* (NASA Document D-15677, JPL, Pasadena, CA, 1998), p. 137.
- [4] R.A. Wilkinson, G.A. Zimmerli, H. Hao, M.R. Moldover, R.F. Berg, W.L. Johnson, R.A. Ferrell, and R.W. Gammon, Phys. Rev. E **57**, 436 (1998).
- [5] G.A. Zimmerli, R.A. Wilkinson, R.A. Ferrell, and M.R. Moldover, Phys. Rev. E **59**, 5862 (1999).
- [6] A. Haupt and J. Straub, Phys. Rev. E **59**, 1795 (1999).
- [7] Y. Garrabos, B. Le Neindre, P. Guenoun, B. Khalil, and D. Beysens, Europhys. Lett. **19**, 491 (1992).
- [8] R.F. Berg, M.R. Moldover, and G.A. Zimmerli, Phys. Rev. Lett. **82**, 920 (1999).
- [9] J.K. Bhattacharjee and R.A. Ferrell, Phys. Rev. A **27**, 1544 (1983).
- [10] J.K. Bhattacharjee, R.A. Ferrell, R.S. Basu, and J.V. Sengers, Phys. Rev. A **24**, 1469 (1981). (The crossover function from this reference is also summarized in Appendix A of Ref. [11].)
- [11] R.F. Berg and M.R. Moldover, J. Chem. Phys. **93**, 1926 (1990).
- [12] L. Bruschi and M. Santini, Phys. Lett. A **73**, 395 (1979).
- [13] L. Bruschi, Nuovo Cimento D **1**, 362 (1982).
- [14] Y. Izumi, Y. Miyake, and R. Kono, Phys. Rev. A **23**, 272 (1981).
- [15] R.F. Berg and M.R. Moldover, J. Chem. Phys. **89**, 3694 (1988).
- [16] H. Hao, R.A. Ferrell, and J.K. Bhattacharjee (unpublished); Hao *et al.* used the value $\eta=0.040$ for the exponent η that appears in the correlation function to obtain $z_\eta=0.066$. We used the value $\eta=0.035$ (see [39,40]) in their expressions to obtain $z_\eta=0.067$.
- [17] R.A. Ferrell and J.K. Bhattacharjee, Phys. Rev. A **31**, 1788 (1985).
- [18] R.F. Berg and M.R. Moldover, NASA Lewis Research Center Document No. 60009-DOC-006, 1993 (unpublished).
- [19] A.M. Peddie, NASA Lewis Research Center Document No. 60009-DOC-014, 1996 (unpublished).
- [20] M.J. Assael, Z.A. Gallis, and V. Vosovic, High Temp.-High Press. **28**, 583 (1996).
- [21] In order to describe materials and experimental procedures adequately, it is occasionally necessary to identify commercial products by the manufacturer's name or label. In no instance does such identification imply endorsement by the National Institute of Standards and Technology, nor does it imply that the particular product or equipment is necessarily the best available for the purpose.
- [22] R.F. Berg, Rev. Sci. Instrum. **66**, 4665 (1995).
- [23] R.F. Berg and M.R. Moldover, NASA Lewis Research Center Report, 1995 (unpublished).
- [24] R.F. Berg, G.A. Zimmerli, and M.R. Moldover, Int. J. Thermophys. **19**, 481 (1998).
- [25] D.W. Oxtoby, J. Chem. Phys. **62**, 1463 (1975).
- [26] I.S. Steinhart and S.R. Hart, Deep-Sea Res. **15**, 497 (1968).
- [27] V.A. Rabinovich, A.A. Vasserman, V.I. Nedostup, L.S. Veksler, *Thermophysical Properties of Neon, Argon, Krypton, and Xenon* (Hemisphere Publishing, Washington, 1987).

- [28] R.F. Berg, NASA Lewis Research Center Report, 1996 (unpublished).
- [29] R.F. Berg, M.J. Lyell, G.B. McFadden, and R.G. Rehm, *Phys. Fluids* **8**, 1464 (1996).
- [30] S.T. Boyd and J. Eraker (private communication).
- [31] *Handbook of Geophysics and the Space Environment*, edited by A.S. Jursa (Air Force Geophysics Laboratory, Washington D.C., 1985), available from the National Technical Information Service, Washington D.C.
- [32] R.F. Berg, *Int. J. Thermophys.* **16**, 1257 (1995).
- [33] R.E. Williams and R.G. Hussey, *Phys. Fluids* **11**, 2083 (1972).
- [34] A.M.J. Davis, *Phys. Fluids A* **5**, 2095 (1993); A.M.J. Davis (private communication).
- [35] U. Narger and D.A. Balzarini, *Phys. Rev. B* **42**, 6651 (1990).
- [36] J. Luettmer-Strathmann, J.V. Sengers, and G.A. Olchow, *J. Chem. Phys.* **103**, 7482 (1995).
- [37] J.V. Sengers and J. Luettmer-Strathmann, in *Transport Properties of Fluids*, edited by J. Millat, J.H. Dymond, and C.A. Nieto de Castro (Cambridge University Press, New York, 1996), Chap. 6.
- [38] J.V. Sengers (private communication).
- [39] H.W.J. Blote, E. Luijten, and J.R. Heringa, *J. Phys. A* **28**, 6289 (1995).
- [40] R. Guida and J. Zinn-Justin, *Nucl. Phys. B* **489**, 626 (1997).
- [41] H. Hao, R.A. Ferrell, and J.K. Bhattacharjee (unpublished).
- [42] E.D. Siggia, B.I. Halperin, and P.C. Hohenberg, *Phys. Rev. B* **13**, 2110 (1976).
- [43] H. Guttinger and D.S. Cannell, *Phys. Rev. A* **24**, 3188 (1981).
- [44] J.K. Bhattacharjee and R.A. Ferrell, *Phys. Lett.* **27A**, 290 (1980).
- [45] W.K.H. Panofsky and M. Phillips, *Classical Electricity and Magnetism* (Addison-Wesley, Reading, MA, 1955).
- [46] K.R. Spangenberg, *Vacuum Tubes* (McGraw-Hill, New York, 1948).
- [47] J.V. Sengers and M.R. Moldover, *Phys. Lett.* **66A**, 44 (1978).
- [48] R. Tofeu, B. Le Neindre, and P. Bury, *C. R. Seances Acad. Sci., Ser. B* **273**, 113 (1971).